SYNTHESIS AND CHARACTERIZATION OF INTERMETALLIC COMPOUNDS AND TRANSITION METAL NITRIDES AS HIGH-PERFORMANCE PROTON EXCHANGE MEMBRANE FUEL CELL MATERIALS

A Thesis
Presented to the Faculty of the Graduate School
of Cornell University
In Partial Fulfillment of the Requirements for the Degree of
Master of Science

by
WEITIAN ZHAO
AUGUST 2014

ABSTRACT

One of the major challenges in fuel cell technologies, particularly for Proton Exchange Membrane Fuel Cells (PEMFCs), is developing effective catalysts for use in both the anode and cathode. Ordered intermetallic compounds have shown considerable potential for fuel cell applications due to their enhanced catalytic activity, better durability and lower cost. In this work, Pd-Sn intermetallic compounds were investigated. PdSn and Pd_3Sn nanoparticles were synthesized under air-free conditions and were tested for their electrochemical properties. Both materials showed poor activities in acidic environment for formic acid and methanol oxidation, but enhanced activities under basic conditions. Various electrochemical tests and structural characterization including high-resolution TEM/STEM and EDX were performed to investigate the changes in these materials that might have resulted in such performance.

In this thesis, we also focus on developing stable catalyst supports for fuel cell electrodes, another topic in fuel cell research. Motivated by recent studies which revealed the potential of transition metal nitrides as high performance catalyst supports, we developed a facile synthesis of single-phase, nanocrystalline macroporous chromium nitride and chromium titanium (oxy)nitride with an inverse opal morphology. Characterization using XRD, SEM, HR-TEM/STEM, TGA and XPS is reported. Interconversion of macroporous CrN to Cr_2O_3 and back to CrN while retaining the inverse opal morphology was also demonstrated.

BIOGRAPHICAL SKETCH

Weitian Zhao was born on August 18th, 1989 in Zhengzhou, China. From the early school years he developed a strong interest in math and astronomy. Through readings and studies, he also gradually became interested in physics. During middle school, Weitian moved to Beijing with his parents and later attended Beijing No. 8 high school, where he participated in many state-level and national-level competitions in math and physics and won many awards. Weitian attended Tsinghua University from 2008 to 2012 majoring in Materials Science and Engineering. His undergraduate research mainly focused on materials chemistry. He also spent a semester at Purdue University as an exchange student in his junior year. After graduating from Tsinghua, Weitian came to Cornell University for a master's degree also in Materials Science and studied under the guidance of Professor Frank DiSalvo and Professor Héctor Abruña. His interest mainly lies in the area of energy materials.

ACKNOWLEDGMENTS

I would like to thank my parents for their invaluable support and giving me all the opportunities in life. I would like to thank my advisor Professor Frank DiSalvo for his help in my studies and research. It is a great pleasure having him, a knowledgeable scientist and a kind gentleman, as my advisor. I would also like to thank my colleagues, especially Douglas DeSario, Dr. Zhiming Cui and Ryo Wakabayashi for their support and helpful discussions. I also greatly appreciate the guidance from Professor Héctor Abruña, particularly on electrochemistry.

The experimental work in this thesis was supported by the Basic Energy Sciences Division of the Department of Energy through Grant DE-FG02-87ER45298 and National Science Foundation (NSF) Materials Research Science and Engineering Centers (MRSEC) program (DMR-1120296).

TABLE OF CONTENTS

Chapter 1

Fuel Cells

1.1 Introduction

The promise of a highly-efficient and clean energy production method has made fuel cell a popular topic over the years. Compared to traditional and widely used energy conversion technologies such as combustion of fossil fuels, the operation of fuel cells divides the direct combustion into two separate half reactions, the oxidation of fuel and the reduction of oxygen, and can convert chemical energy directly into electrical energy.[1] The efficiency of this process is not limited by the Carnot cycle for heat engines. Theoretically, close to 100% of the reaction Gibbs free energy can be harnessed.

Various types of fuel cells have been developed with respective strengths and weaknesses. In general, fuel cells operating at a lower temperature suffer from slow reaction kinetics and require the use of expensive catalysts. However, the low operation temperature and the quick start-up features also make it more suitable for portable applications compared to high-temperature fuel cells such as Solid Oxide Fuel Cells (SOFC), which typically operate at over 700ºC.

1.2 Proton Exchange Membrane Fuel Cell

The Proton Exchange Membrane Fuel Cells (PEMFCs) operate at relatively low temperatures (80ºC) and have higher power density compared to other types of fuel cells.[2] These features make them promising candidates for portable power sources and for example can be used to replace thermal engines in automobiles.

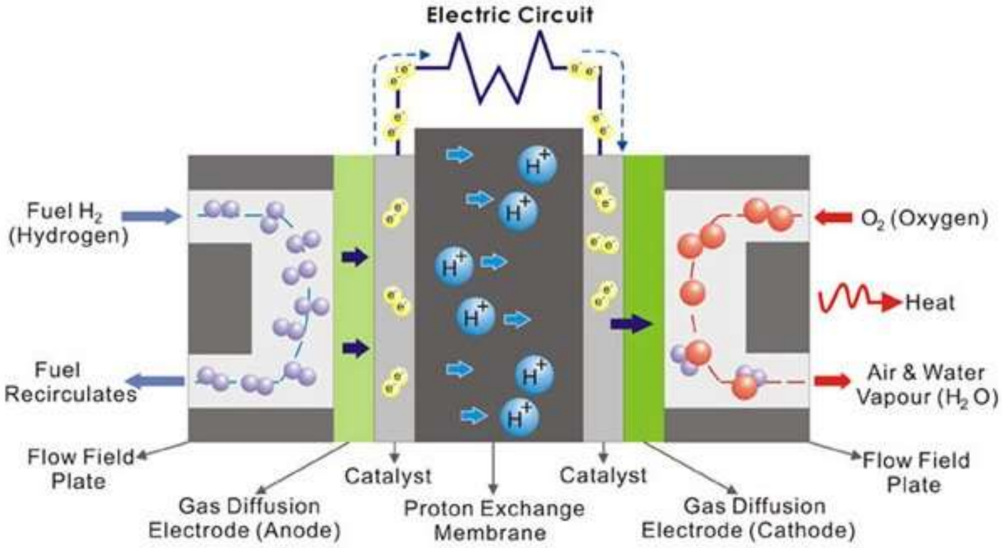

Figure 1.1, Proton Exchange Membrane Fuel Cell.[3]

Figure 1.1 shows a typical PEMFC. In the anode, the fuel, in this case, hydrogen, is oxidized and electrons are forced to go through the external circuit to react with oxygen at the cathode, while the protons can cross the membrane to the cathode. At the cathode, oxygen is reduced and combined with protons to form water, which is the only product of the reaction. The cathode reaction is called the Oxygen Reduction Reaction (ORR). At an operating temperature of 80ºC, these reactions need to be catalyzed to occur at reasonable rates and thus catalysts, mostly platinum-based materials, are used in both electrodes. Catalyst supports are also used to maximize the electrical contact of catalyst to the current collector so that charge can flow through the external circuit from one electrode to the other.

1.3 Major materials challenges for PEMFC

One of the major materials challenges for PEMFC is the effectiveness of the catalyst materials in catalyzing the ORR as well as the oxidation of fuels other than hydrogen. The oxidation of hydrogen is a much faster process compared to ORR. But since hydrogen exists as a gas at ambient conditions, the storage and transportation issues make it less favorable to be used as fuels. Thus, the use of liquid fuels, for example Small Organic Molecules (SOMs), such as methanol or ethanol, is desired. Previous research has been focused on the search for more effective electrocatalysts for these fuels, since Pt can be easily poisoned by the byproducts of the reaction such as CO, especially at low potentials, greatly slowing the oxidation of the fuel.

Another important challenge in fuel cells is the durability of the catalyst supports during the operation of fuel cells. The currently used carbon black supports oxidize to CO_2 especially when the fuel cell is rapidly cycled in power output or when first starting the fuel cell. The degradation of the support materials can cause aggregation of catalysts, which will dramatically lower the catalytic activity, since surface area is lost on agglomeration. All these issues demand development of new effective and stable materials for both catalysts and supports.

1.3.1 Intermetallic compounds as high-performance fuel cell electrocatalysts

Due to their unique electronic structure, Pt and Pt-based materials are used as catalysts at both the anode and cathode. Despite extensive efforts in the area to replace this expensive material, non-precious metal catalysts, such as certain perovskites, are still not comparable with Pt catalysts, in terms of catalytic activities.[4] However, by alloying Pt with another element, enhanced activities can be obtained.[5] A search for various high-performance Pt-based materials were conducted in the past few years and many of these materials have been reported by the DiSalvo group.

Rather than alloys, in which the atomic positions are occupied randomly according to the alloy composition, we are more interested in synthesizing ordered intermetallic phases, where each atom occupies its own crystallographic position. The advantage of the ordered phase is its better durability compared to most if not all alloys . In the acidic environment of a PEMFC, the M in $Pt_{1-x}M_x$, with M such as Fe, Sn, Co will leach out to the solution at high potentials or in oxidizing acids, leaving a Pt-rich shell and an intermetallic core. The Pt shell is the active catalyst, but the strain caused by an intermetallic core will slightly change the electronic structure thus the adsorption strength with different intermediates of the reaction, sometimes reducing the Pt-CO bond strength and increasing the catalytic activity. In addition, the replacement of some Pt atoms with M also lowers the cost. Besides Pt-based alloys and intermetallic compounds, efforts were also made to find effective Pd-based catalysts.

1.3.2 Transition metal nitrides as high performance fuel cell supports

As discussed above, high surface area catalyst supports were used to maximize the utilization of expensive catalysts. Presently, carbon black is chosen for this role in PEMFC due to its high surface area, good electrical conductivity and the ability to disperse and bind catalyst particles. However, carbon-based materials are not thermodynamically stable even at modest operation potentials (> 0.4V) and corrosion (oxidation) can happen, which causes sintering of catalysts and loss of activity. Hence stable, conductive and high surface area materials are needed to replace the carbon black.

Metal nitrides have been widely used in industry due to their high wear resistance, high hardness and good thermal stability.[6] Besides, most of transition metal nitrides are good electrical conductors and are very resistant to corrosion.[7] These properties make them promising candidates for catalyst supports. Studies of nitride materials as high-performance PEMFC catalyst supports have been reported and a comparable catalytic activity and stability compared to conventional carbon black supported catalysts were observed.[8] Some of these past studies were conducted in the DiSalvo group and motivated part of this thesis work.

REFERENCES

[1] Steele, B.; Heinzel, A. *Nature*, **2001**, 414, 345-352.

[2] Subban, C. V. Synthesis and Characterization of Mixed-Metal Oxides for Catalyst Support Applications in Proton Exchange Membrane Fuel Cells. Doctoral dissertation, Cornell University, Ithaca, NY, August 2012.

[3] Proton Exchange Membrane Fuel Cell (PEMFC), Available online: http://www.g-energy.com.my/fuel_cell_tech_PEMFC.html, accessed: 05/12/2014.

[4] Suntivich, J.; May, K. J.; Gasteiger, H. A.; Goodenough, J. B.; Shao-Horn, Y. *Science*, **2011**, 334, 1383-1385.

[5] Wang, D.; Xin, H. L.; Hovden, R.; Wang, H.; Yu, Y.; Muller, D. A.; DiSalvo, F. J.; Abruña, H. D. *Nature Mat.*, **2013**, 12, 81-87.

[6] Toth, L. E. *Transition Metal Nitrides and Carbides*; Academic Press: New York, 1971.

[7] Oyama, S. T. *The Chemistry of Transition Metal Carbides and Nitrides*; Springer: London, 1996.

[8] Yang, M.; Guarecuco, R.; DiSalvo, F. J. *Chem. Mater*. **2013**, 25, 1783-1787.

Chapter 2

Pd-Sn Intermetallic Compounds as Fuel Cell Electrocatalyst. Part I: Synthesis Method

2.1 Overview of synthesis method of intermetallic compounds

Traditionally, intermetallic compounds can be synthesized via high temperature reactions, where atoms have a sufficient diffusion rate to mix together. This reaction is also scalable and thus is widely used in industry. However, the need for nano-sized and high surface area materials for catalysis spurs research in low-temperature solution-based synthesis, in which different metals are reduced from their respective metal salts to form nanoparticles. These nanoparticles typically need to be annealed later in order to obtain an ordered intermetallic phase. The nanoparticle catalysts can be later transferred onto carbon black to make a catalyst. Figure 2.1 shows a typical synthesis scheme for intermetallic nanoparticle catalysts. It should be noted that the process is typically conducted under air-free conditions, such as in glove box, to prevent possible oxidation of metals, particularly those more oxyphilic elements, such as Sn, Mn and Ti.

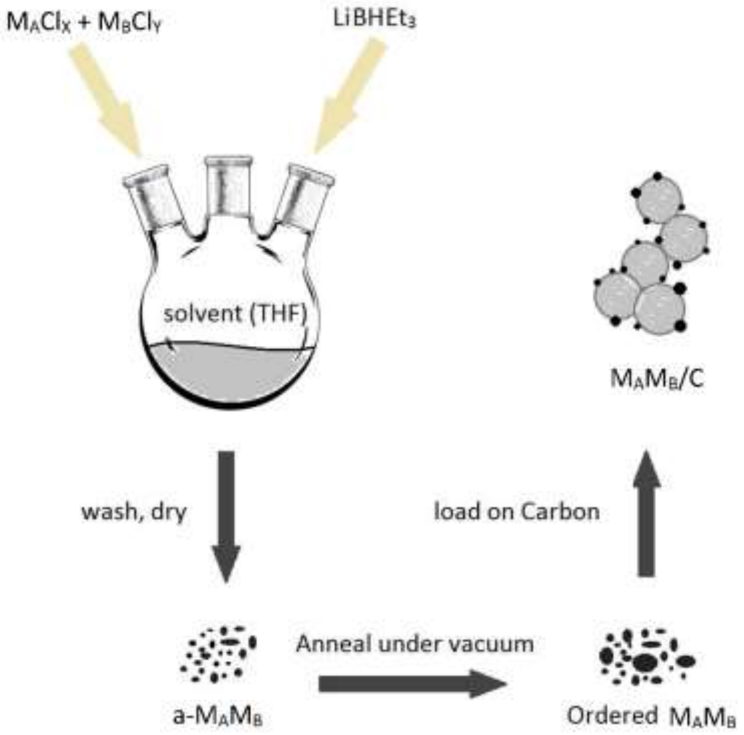

Figure 2.1. Synthesis procedure of ordered intermetallic compounds.

In this typical synthesis process, metal chloride precursors are first dissolved in tetrahydrofuran (THF) followed by continuous stirring. Later, a strong reducing agent ($MBHEt_3$ with M = Li or K) is added to simultaneously reduce metal A and metal B. After some time of stirring, the product is washed and sealed under vacuum to be annealed at 200 - 800ºC to hopefully form an ordered intermetallic phase. The last stage is transferring the nanoparticles onto a carbon black support.

In the process, the choice of solvent, metal precursor as well as reducing agent are worthy of a discussion. In our lab, we often choose THF as it is stable at very reducing potentials, can dissolve a wide variety of appropriate metal precursors, and typically does not react with very oxyphilic elements to form oxides or hydroxides, as does water or ethanol for example. In order to form nano-sized intermetallic particles, it is desired to form a well-mixed product rather than having a phase separation. This requires a strong reducing agent such as $LiEt_3BH$ or KEt_3BH which can simultaneously and rapidly reduce all the elements of interest. A typical reaction can be written as follows:

$$3PtCl_4 + FeCl_3 + 15LiEt_3BH \rightarrow Pt_3Fe + 15LiCl + 7.5H_2 + 15Et_3B \qquad \text{(Equ. 2.1)}$$

In this case, all products except Pt_3Fe are soluble in THF.

Besides the solvent, the other variable in the synthesis is the choice of metal precursors. From the previous experience in the group, the use of organic precursors such as $Pt(acac)_2$ will lead to carbon coating of the intermetallic nanoparticles after annealing, which blocks the active surface sites and dramatically reduces the electrochemical activity.[1] Thus we have switched to the use of inorganic precursors including metal chlorides such as $PtCl_4$ and $PdCl_2$. By adding LiCl, the solubility of these precursors in THF can be increased.

Many variations of above-mentioned synthesis also exist. By adding carbon black to the solution before the reduction happens, intermetallic compounds can be directly reduced onto the support. The other variation is to use KEt_3BH as the reducing agent, which results in an insoluble byproduct of KCl, which precipitates out of the solution and serves as a matrix to trap the nanoparticles from agglomerating and growing during any later annealing processes.[2] Different synthesis methods were used in this thesis work and will be discussed in more detail later.

2.2 The synthesis of PdSn and Pd_3Sn intermetallic compounds

The work on Pt-Sn intermetallic compounds and the need for exploring Pd-based catalysts motivated the study of Pd-Sn intermetallic catalysts. Figure 2.2 is the phase diagram of Pd-Sn binary system. Although this phase diagram may be modified for materials with sizes in the nanoscale region, it provides some knowledge in terms of difficulty in obtaining certain intermetallic phases, as diffusion rates in a given family of materials with same structure tend to scale with the bulk melting point.[3] Also, congruently melting phases are in general easier to prepare as nanoparticles compared to incongruently melting phases.

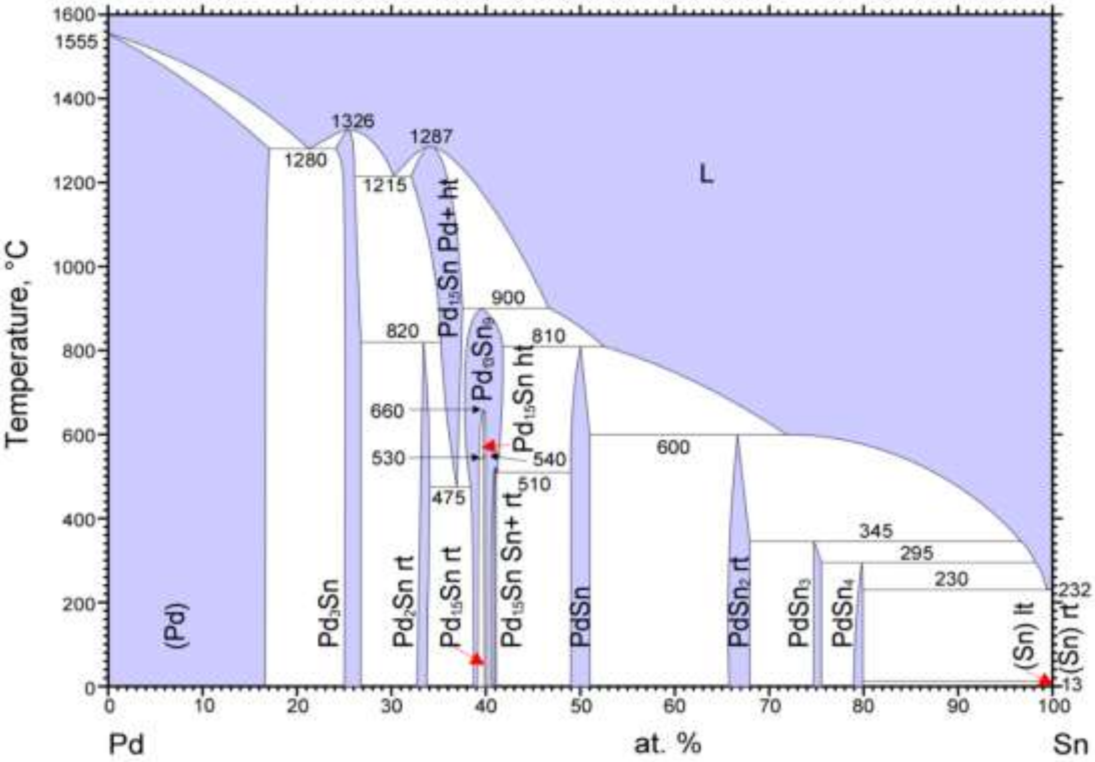

Figure 2.2. Phase diagram of Pd – Sn.

2.2.1 Synthesis of Pd_3Sn intermetallic nanoparticles (NPs)

$PdCl_2$, $SnCl_2$ and LiCl in the molar ratio of 3:1:12 were dissolved in 20 mL THF followed by continuous stirring. The process was carried out in an argon-filled glove box to prevent the possible oxidation of Sn. After stirring for 2 hours, an appropriate amount (to make a 20 wt. % total metal loading) of carbon black was added into the solution. The solution was stirring for half an hour before drawn up by a syringe to inject slowly into the reducing agent of 50% excess $LiEt_3BH$ under vigorous stirring. The mixture immediately turned into an opaque black suspension. After continued stirring for about 10 minutes, the sample was washed under air-free conditions for two times using THF and one time using hexane. Then the samples were dried and sealed under vacuum in silica tubes for annealing at different temperatures. An annealing time of 24 hours is used in all cases. After annealing and cooling, the samples were allowed to be exposed to air and were tested by X-Ray Diffraction (XRD).

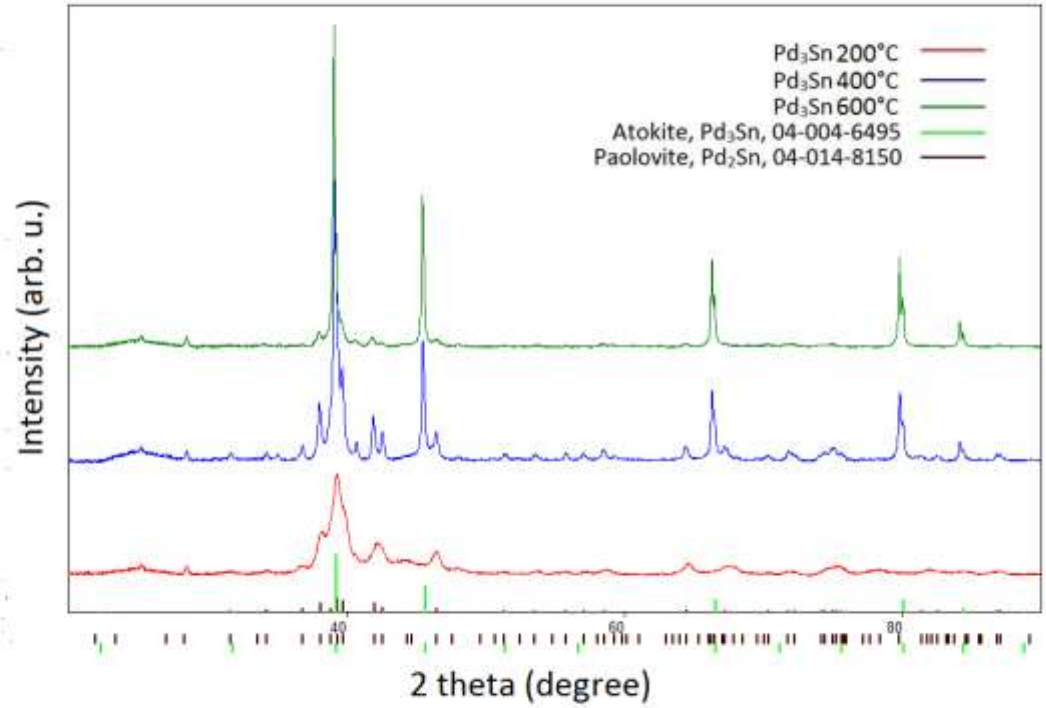

Figure 2.3. XRD patterns of Pd_3Sn sample annealed at different temperatures.

It can be seen in Figure 2.3 that an evolution of phases was observed. At lower annealing temperature (200ºC), the XRD pattern matches with the reported Pd_2Sn pattern plus an extra bump around 40º indicating an amorphous component. With increasing temperature, the Pd_3Sn phase gradually grows and become the dominant phase. The phase evolution might be attributed to the diffusion of amorphous Pd in the as-made samples. Note that the reduction potential of $Sn^{2+} \rightarrow Sn$ is -0.1375V with $Pd^{2+} \rightarrow Pd$ having a much higher reduction potential at 0.915V.[4] It is possible that Pd was more readily reduced during the reduction process and results in first forming a Pd-rich amorphous product. None of the attempts to synthesize completely pure Pd_3Sn phase succeeded. In most cases a slight amount of Pd_2Sn phase is present.

The ordered arrangement of different atoms leads to ordering peaks which do not show up in XRD patterns in the case of alloys and can be used in identifying ordered intermetallic compounds. However, for the Pd-Sn system, the small Z contrast (46 for Pd and 50 for Sn) results in similar scattering abilities. For Pd_3Sn with a Face-Centered Cubic (FCC) cell, no ordering peaks were reported in the standard PDF cards. This posed a problem in identifying ordered intermetallic compounds from the room temperature Pd_3Sn alloy. The small difference in atomic number is also a problem for using other techniques such as Electron Energy Loss Spectroscopy (EELS) for identification. In this case, it is not certain that an ordered phase was obtained.

2.2.2 Synthesis of PdSn intermetallic NPs

Orthorhombic PdSn was made by two different methods. The sample made by reduction of metal salts in the presence of carbon black is denoted as PdSnC and the sample made using KEt_3BH and later transferred to carbon black is denoted as PdSn-C. For PdSnC, the synthesis procedure is the same as previously described for Pd_3Sn except that the molar ratio of the Pd and Sn precursors is 1:1. For the PdSn-C sample, KEt_3BH was used instead of $LiEt_3BH$ and carbon black was no longer involved before the reduction. Samples of the resulting KCl NP composite were annealed at different temperatures. The product was later transferred onto carbon black using ethylene glycol following the suggested method.[2] In this process, carbon black was sonicated using a solid sonicater (Microson ultrasonic cell disruptor XL) with ethylene glycol for ~5 minutes to form a uniform suspension. Then the suspension was added to the scintillation vial with PdSn-KCl powders, and then sonicated using solid sonicater for about 10 minutes. The suspension was centrifuged and the supernatant was removed. The product was washed by distilled water for three times and finally was dried in a furnace for further characterization.

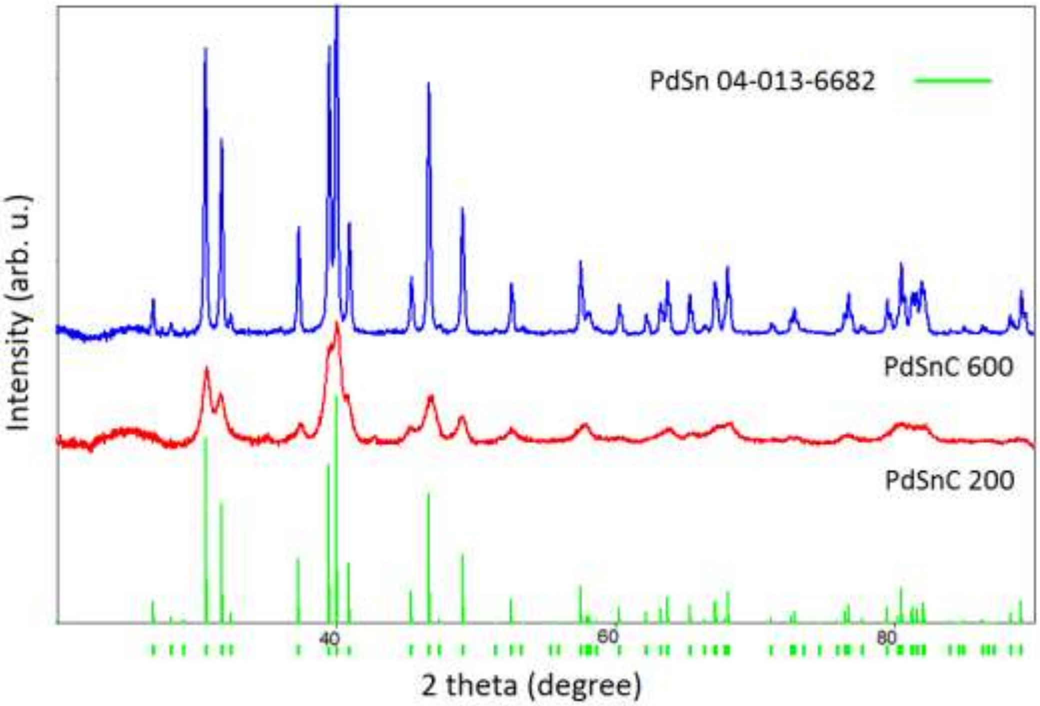

Figure 2.4. pXRD patterns of PdSnC synthesized at different temperatures.

The figure above shows the XRD patterns for PdSn nanoparticles synthesized by the reduction in the presence of carbon black. It can be seen that the XRD pattern of PdSn annealed at 200ºC matches well with reported single phase PdSn (orthorhombic structure, MnP type). As expected, annealing at a higher temperature at 600ºC for the same amount of time (24 hours) increases the domain size of the particle and results in narrower peaks. After calculation using Halder-Wagner method, the domain size increased from 2.4 nm to 39.6 nm. This big difference is possibly due to the lack of protecting layers between the as-synthesized nanoparticles, since no organic ligands or any other insoluble matrix was involved during the synthesis. The PdSn samples prepared by the KCl method can also be matched with the same PdSn phase but contains extra peaks from KCl.

Table 2.1 lists the calculated average domain sizes of different samples. In this experiment, the effect of KCl in suppressing the NP crystal growth and controlling the domain size is not seen as the PdSn-C 600 sample grows to crystals with the highest average domain size. This might be caused by the relatively small amount of KCl used in the experiment. The synthesized materials, PdSnC 200 and Pd_3SnC 600 were tested for their electrochemical activities which are shown in later chapters.

Table 2.1. Phase and domain size of different Pd_xSn samples.

Sample	Phase	Domain size (calculated by XRD)
PdSnC 200	PdSn	2.4 nm
PdSnC 600	PdSn	39.6 nm
PdSn-C 200	PdSn	14.7 nm
Pd_3SnC 600	71% Pd_3Sn, 29% Pd_2Sn	38.0 nm (Pd_3Sn)

REFERENCES

[1] Leonard, B. M.; Zhou, Q.; Wu, D.; DiSalvo, F. J. *Chem. Mater*., **2011**, 23, 1136-1146.

[2] Chen, H.; Wang, D. L.; Yu, Y.; Newton, K. A.; Muller, D. A.; Abruña, H. D.; DiSalvo, F. J. *J. Am. Chem. Soc.* **2012**, 134, 18453−18459.

[3] Antczak, G.; Ehrlich, G. *Surf. Sci. Rep*. **2007**, 62, 39−61.

[4] Bard, A. J.; Faulkner, L.R. *Electrochemical Methods: Fundamentals and Applications*; Wiley, 2001.

Chapter 3

Pd-Sn Intermetallic Compounds as Fuel Cell Electrocatalysts Part. II: Characterization

3.1 Electrochemical properties of Pd-Sn$_x$ intermetallic compounds

3.1.1 Properties of Pd-Sn$_x$ intermetallic compounds in an acidic environment

Achieving an enhanced electrochemical property is the ultimate goal for the search and synthesis of ordered intermetallic compounds. Since PEMFCs operate in an acidic environment, the electrochemical activities of as-made PdSn and Pd_3Sn were first measured under acidic conditions, in 0.1M $HClO_4$ at room temperature using a three-electrode cell setup. 5mg of catalyst (20% metal loading) was mixed with 1mL Ethanol and 50μL Nafion solution (5 wt. %) to make an ink. Then 10 μL of this ink was dropped onto a glassy carbon electrode and dried to make an electrode. Before the loading of catalyst, the glassy carbon electrode was polished for over 5 minutes and sonicated using water bath for 1 minute. The cell was de-aired by flowing argon gas through the cell for over 20 minutes before each experiment.

Pd_xSn samples were tested for formic acid oxidation. As a comparison group, pure Pd (domain size of 9 nm by XRD) was also tested. As shown in Figure 3.1, Pd_3SnC 600 and PdSnC 200 samples have very little activity toward formic acid oxidation compared with Pd. This is also seen in PdSn samples made using the KCl method and samples made with different annealing temperatures. All the samples were also tested for their activity for methanol and ethanol oxidation in the same acidic condition. Similar results of poor activity compared to pure Pd were observed.

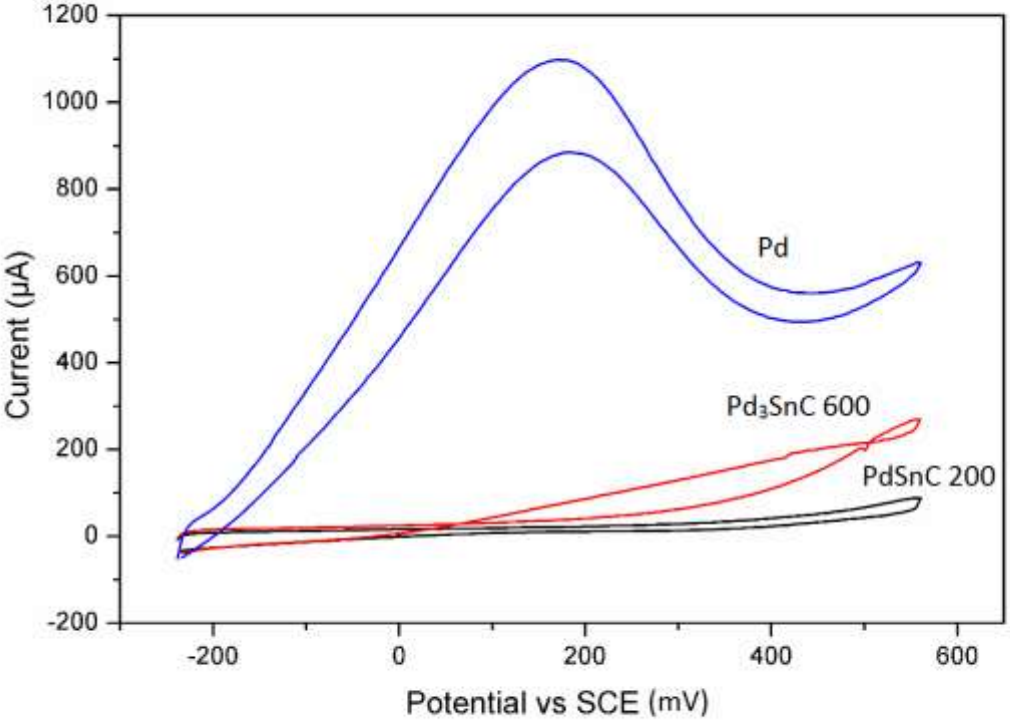

Figure 3.1. Cyclic Voltammogram (CV) of Pd, Pd_3SnC and PdSnC in 1M formic acid and 0.1M $HClO_4$.

3.1.2 Properties of Pd-Sn_x intermetallic compounds in a basic environment

The samples were further tested in a basic environment using 1M NaOH. The Pd sample showed a steady performance as the potential cycled between 0V to 1V versus the Standard Hydrogen Electrode (SHE). However, all the Pd_xSn samples showed a gradually increasing activity as the potential cycles. Finally, the activity will stabilize, and the activity was higher than Pd. Typical CVs recorded for the PdSnC 200 sample for formate oxidation are shown below.

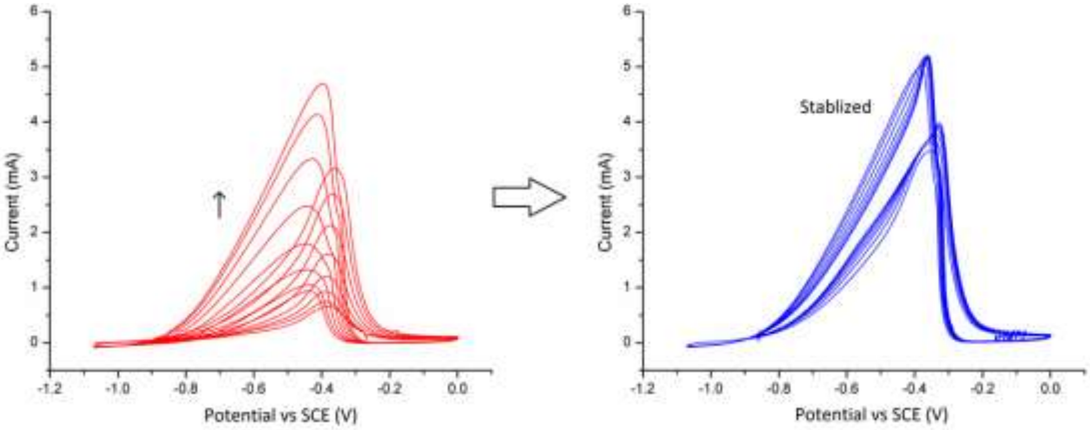

Figure 3.2. CV behavior of PdSnC 200 sample in 1M formate and 0.1M $HClO_4$.

To accurately determine the electrochemical activity of the materials, normalization using the Electrochemical Surface Area (ECSA) is needed, which can be calculated by a CO stripping experiment. In this experiment, CO was bubbled to the solution and adsorbed onto the surface of the electrode, which can then be removed electrochemically by oxidization at a higher potential. The amount of CO oxidized can be calculated from the area under the CO oxidation peak, and is proportional to the ECSA. Comparisons with Pd samples with different domain size, achieved by annealing the reduced Pd product at different temperatures, were conducted. These two Pd samples were synthesized by reducing $PdCl_2$ with $LiEt_3BH$ and later transferred onto carbon black. Table 3.1 gives the information of samples used in the CO stripping experiment.

Table 3.1. Phase and domain size of different Pd, PdSn and Pd_3Sn samples.

Sample	Phase	Domain size (from XRD)
Pd-1	Pd	4.1 nm
Pd-2	Pd	6.4 nm
PdSnC 200	PdSn	2.4 nm
Pd_3SnC 600	71% Pd_3Sn, 29% Pd_2Sn	38.0 nm

The data of CO stripping measurements is shown in Figure 3.3.

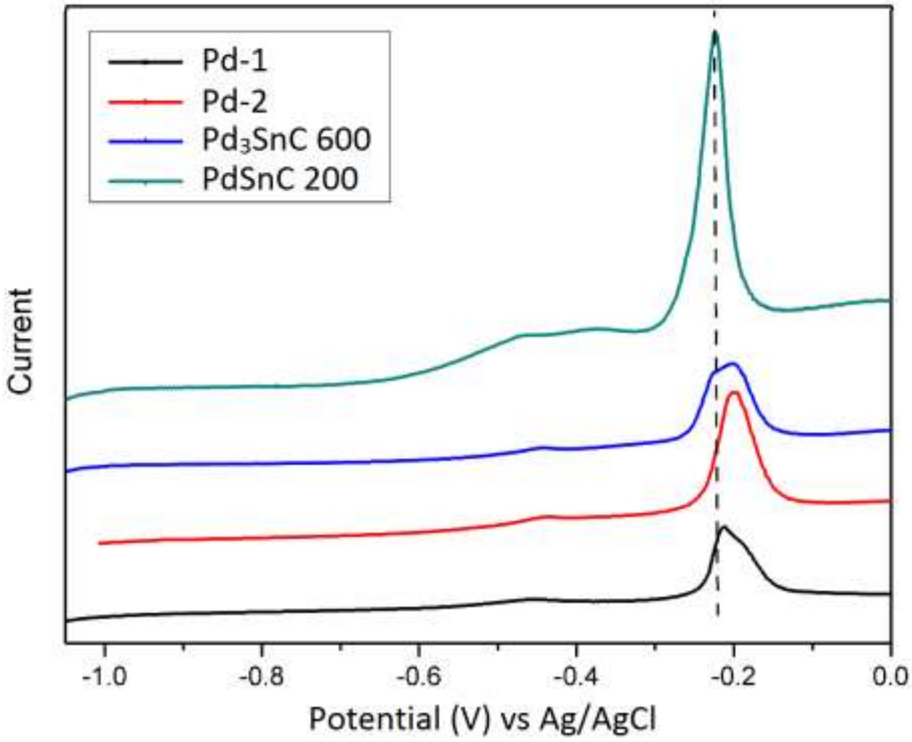

Figure 3.3. CO oxidation curve of Pd, Pd_3Sn and PdSn.

Comparing the peak position for CO oxidation, we see that PdSn has a slightly lower oxidation potential for CO, compared with Pd_3Sn and Pd. After dividing the activity by the ECSA, the normalized activity toward methanol for PdSnC 200, Pd_3SnC 600 and Pd can be determined.

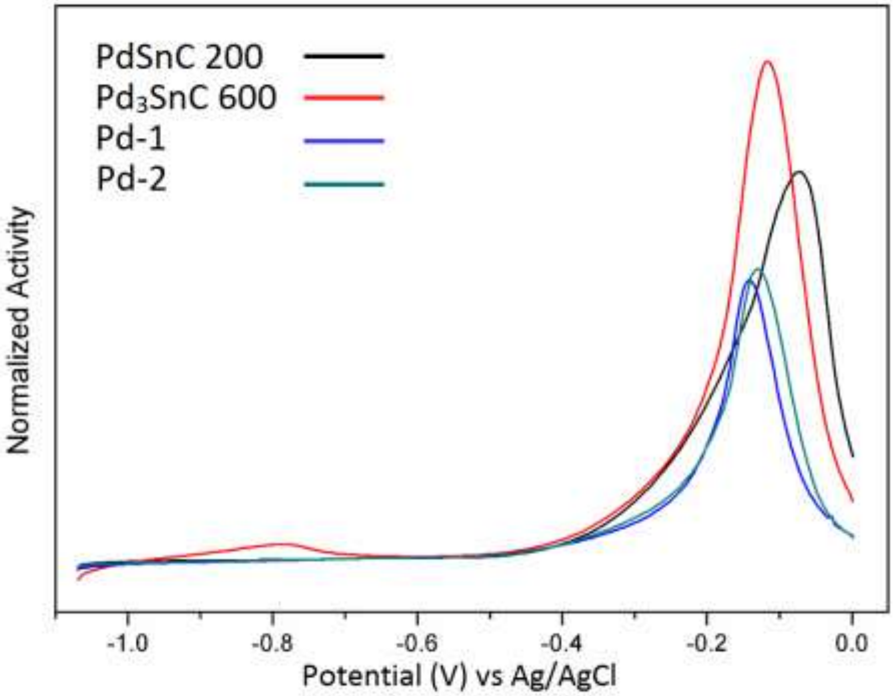

Figure 3.4. Normalized activity toward methanol in 1M NaOH, calculated using ECSA from CO stripping measurement.

Figure 3.4 shows the difference in activity of different samples for methanol oxidation in base. It can be seen that both Pd_3Sn and PdSn intermetallic compounds show better activity compared with Pd and Pd_3Sn shows the best performance. As expected, after considering the ECSA, the activity as well as onset potential for the same material (Pd) is very similar, which also proves that Pd-Sn intermetallic compounds have higher activities for methanol oxidation in base.

3.2 Structural characterization of intermetallic compounds before and after electrochemical tests

To better understand the cause for poor activity in acid but enhanced activity in base, high resolution structural characterization was carried out. The gradually changing activity in the CV experiment also suggested that the activity changes were likely caused by possible surface changes in the materials, rather than a change caused by different reaction routes in acid and base conditions. Using sample PdSnC 200, EDX data was collected before and after repeated (overnight) electrochemical scans from 0.0 to 1 V vs SHE.

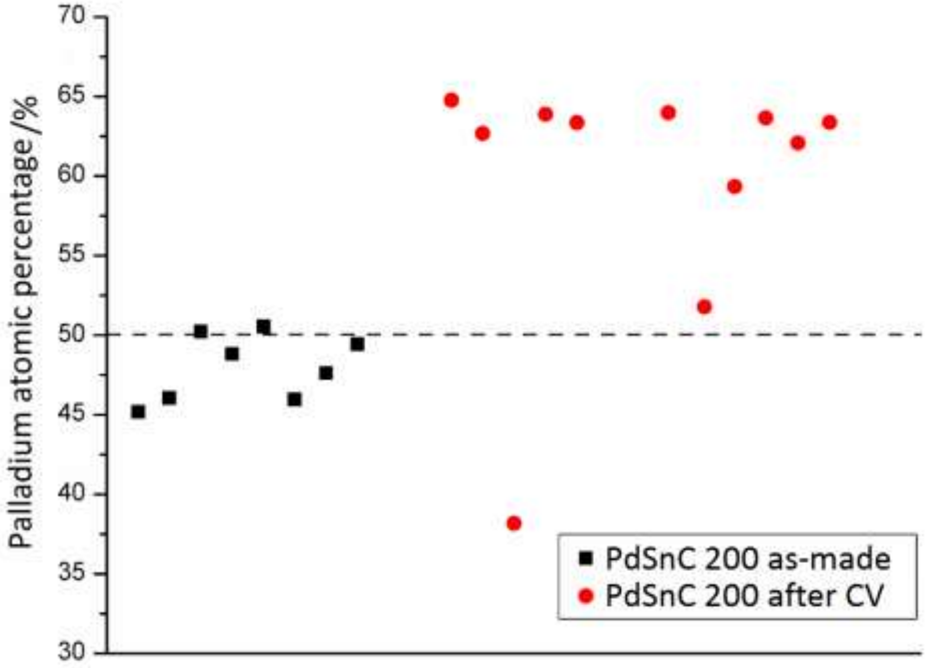

Figure 3.5. EDX data of Pd content for as-made and tested PdSn.

Figure 3.5 shows the EDX data collected by a field emission SEM. Despite possible instrumental errors, the data collected showed a clear change in palladium atomic percentage after repeated (overnight) electrochemical measurements.

High-resolution bright field TEM images were taken trying to observe the direct evidence for structural changes and is shown in Figure 3.6.

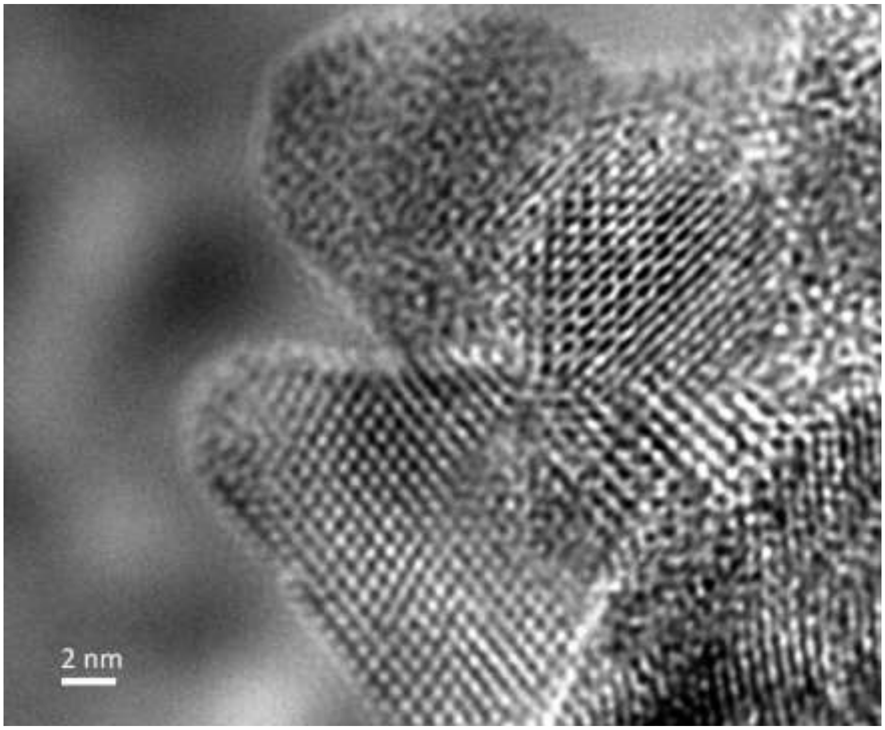

Figure 3.6. BF HR-TEM image of PdSnC 200 after electrochemical tests.

In spite of apparent changes in atomic percentage of Pd, it is difficult to determine from this TEM image. We assumed a cubic crystal of N atoms across, and that the surface is composed of half Pd and half Sn. If all the Sn atoms on the surface were leached out to the solution, the loss of surface atoms will be: $(N^3-(N-2)^3)/2 = 3N^2 - 6N + 4$. The Pd composition will change to $(N^3/2)/(N^3-(3N^2 - 6N + 4))$. We further assume this value to be 62.5%, which is a rough average from the EDX data. It can be calculated that $N \approx 13$. This means that the loss of Sn from only the top layer of a crystal that is 13 atoms across is sufficient to increase the Pd content from 50% to 62.5%. Thus it is very difficult to tell from the TEM image whether there are any changes in the monolayer on the surface.

HAADF images with high-resolution EDX line scans were also performed for sample Pd_3SnC 600. The result is shown in Figure 3.7.

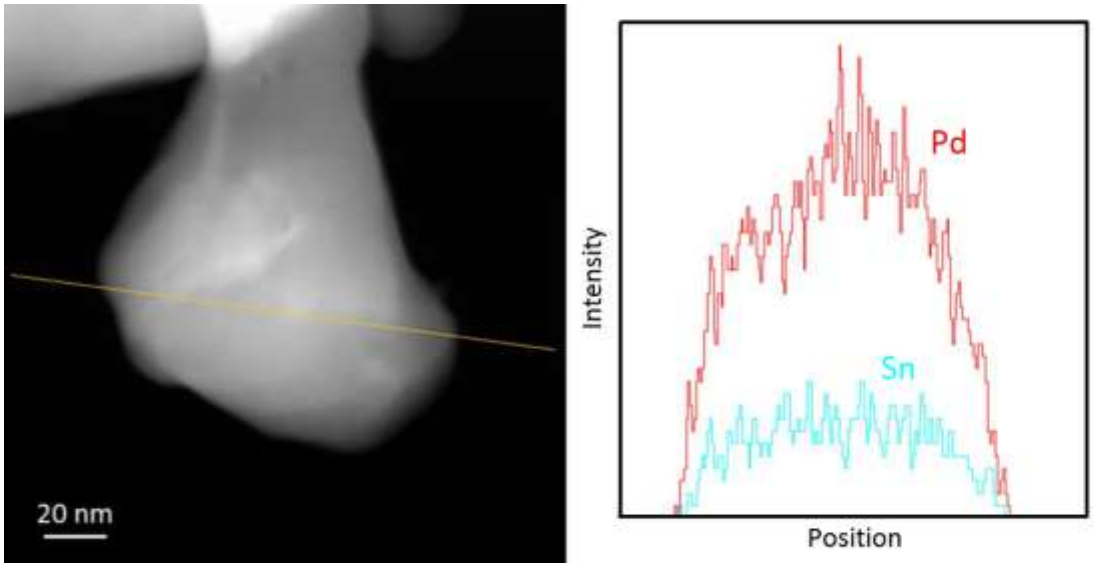

Figure 3.7. HAADF image with an EDX analysis showing the Pd, Sn distribution in a Pd_3Sn particle marked by the yellow line.

Figure 3.7 and many other measurements for different particles did not show the presence of a core-shell structure for Pd_3Sn nanoparticles after the electrochemical measurements. This is likely due to the difference between the 3:1 sample and 1:1 sample as Pd_3Sn sample has larger particles and thus the composition is less sensitive to surface changes.

The chemical state of an element can be affected by the electrical potential as well as the pH in the aqueous environment. This relation is shown in the Pourbaix diagram. However, it should be noted that the Pourbaix diagram is accurate only when a single element is present. In the presence of another element, the behavior will change due to interaction between two elements. In most cases, in the presence of precious metal, the metal/alloy state of transition metal is more stable. However, the Pourbaix diagram can still provide a guide in understanding the possible changes in materials when varying the electrical potential and pH.

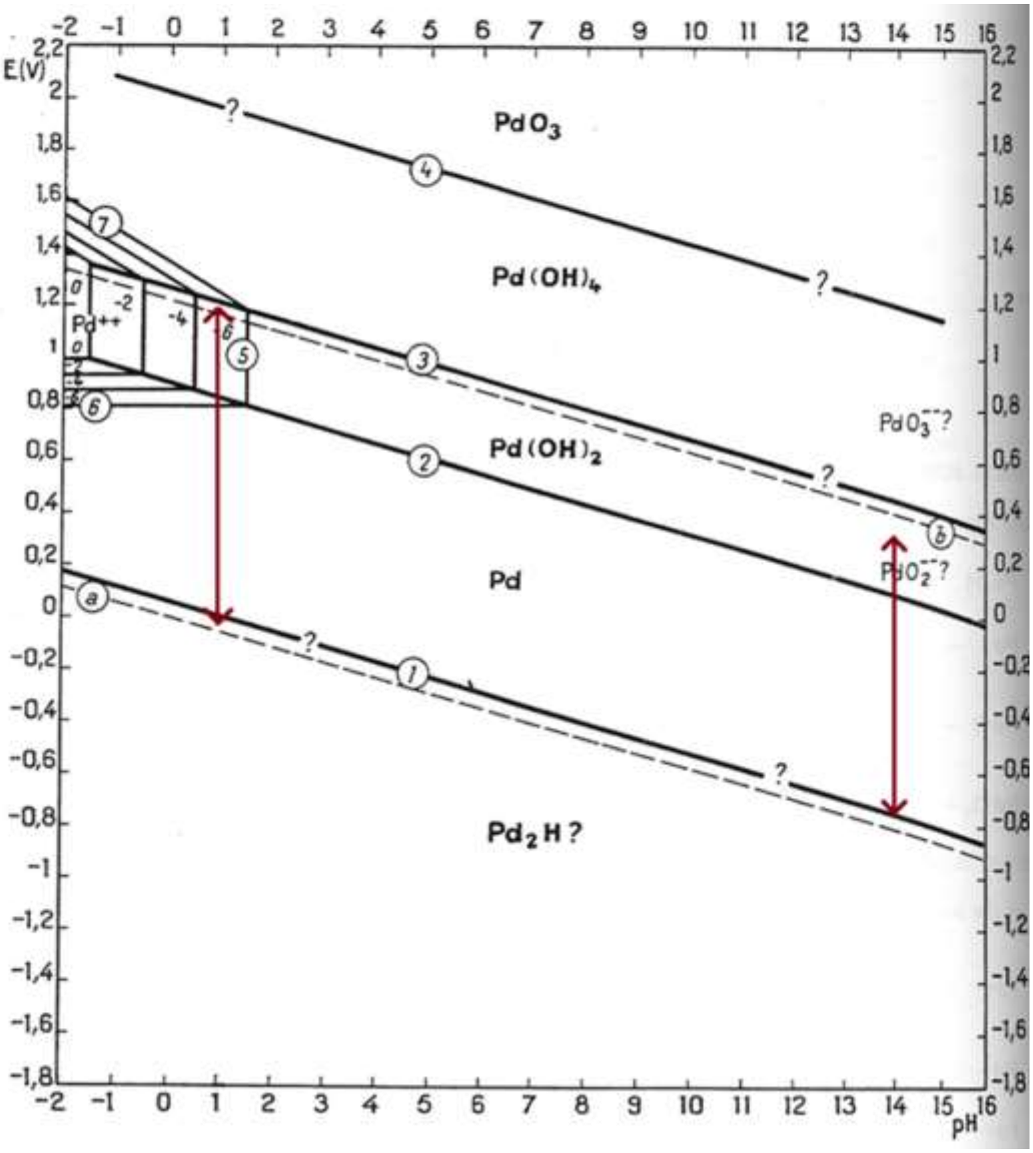

Figure 3.8. Potential-pH equilibrium diagram for the system palladium-water at 25 ºC.

The brown arrows indicate the operating range in the measurements in acidic and basic conditions. Interconversion between Pd and $Pd(OH)_2$ is expected for Pd but possibility of some Pd^{2+} ion dissolving into the solution also exists.

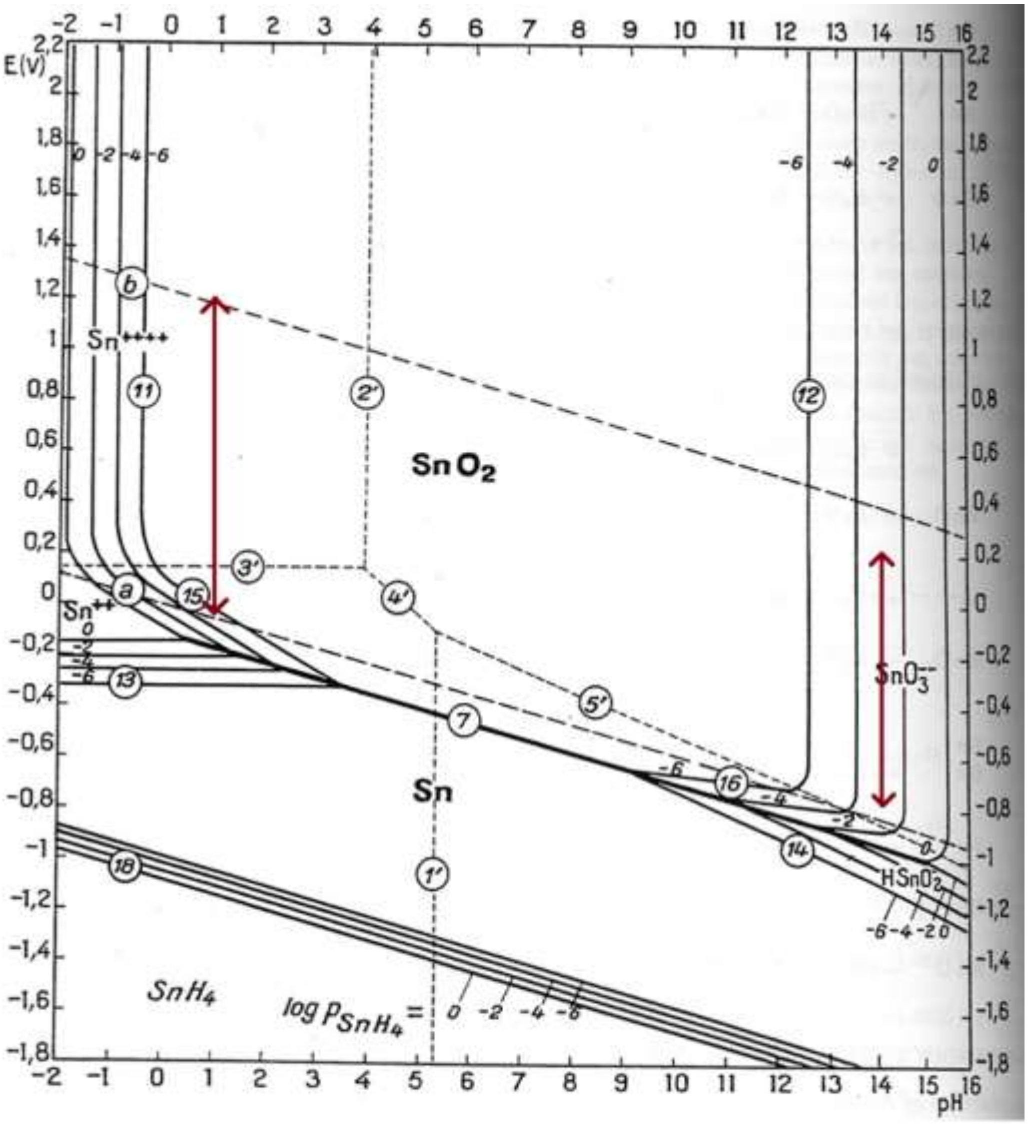

Figure 3.9. Potential-pH equilibrium diagram for the system tin-water at 25ºC. (Considering the anhydrous oxides SnO and SnO_2)

Without Pd, SnO_2 is stable under the operating range at acidic conditions while SnO_3^{2-} might dissolve into the solution in a basic environment. The exact behavior of tin in the presence of Pd cannot be easily determined from these diagrams. However, from the EDX data, it seems that Sn is leaching out to the solution when tested in base. It is also known that tin oxide, SnO_2, and SnO is stable in acid. So it is possible that the leaching of Sn atoms in basic environment causes the enhanced activity while the forming of insoluble SnO_x under acidic conditions inhibits the activity of Pd.

3.3 Conclusions

PdSn and Pd_3Sn were successfully synthesized using solution-based reduction methods. This surfactant-free technique enables a synthesis of clean particle surface, but on the other hand cannot prevent particle growth during relative high temperature (600°C) annealing process required to form the Pd_3Sn phase.

These intermetallic nanoparticles were tested for their activities in electrooxidation of formic acid and methanol in both acidic and basic environments (formate instead of formic acid in the case of base). The results indicate that the catalysts are inactive in acid, while demonstrating a gradually increasing activity in base. Normalized activities derived from CO stripping and CV confirm the superior performance of Pd_xSn intermetallic compounds versus just palladium catalyst.

EDX in SEM shows a reduced Sn content after electrochemical measurements in base for the PdSn ordered intermetallic compound annealed at 200°C. However, possible core-shell structures were not observed by high-resolution EDX analysis in STEM for sample Pd_3SnC 600.

Chapter 4

Ordered Macroporous Chromium Nitride and Chromium Titanium (Oxy) Nitride as Active Fuel Cell Catalyst Support

4.1 Introduction of synthesis of ordered porous transition metal nitride

For applications for catalyst supports, materials with high surface area which maximize the contact with the fuels are desired. Traditional bulk synthesis typically involves high temperature (above 800°C) and high-pressure, which causes significant sintering and produces products with large particle size and low surface area, thus do not meet the requirements for high-performance catalyst support.[1] Many efforts have been made to achieve low-temperature synthesis of nanocrystalline nitrides.[2] In addition to the particle size requirement, interest has been given to making an ordered porous structure. The ammonolysis, i.e. heating under ammonia, of oxides is one of the commonest routes in making nanostructured crystalline nitrides. However, several problems and limitations are associated with this method. a) Oxides tend to sinter easily, making it a challenge to obtain oxides with nano-scale porous morphology. Some literature reports synthesis employing hard templates such as silica or carbon to keep the porous oxide from collapsing, but these templates are often difficult to remove later.[3, 4] Besides, maintaining the morphology during nitridation of the porous oxide is a challenge as the conversion temperature of the thermodynamically favored oxide is reported to be generally very high.[5, 6] In addition, the volume shrinkage upon nitridation may also contribute to the collapse of the pores. b) Ammonolysis of early transition metal oxides above 500°C produces nitrides with the rock salt structure.

However, up to 10% oxygen impurities are present. Such impurities are reduced by processing at higher temperatures, which may again lead to changes in morphology. c) It is difficult to produce mixed metal nitrides of different stoichiometries as oxide precursors with a variable metal stoichiometry are generally not available, thus greatly limiting the applicability of that method.

For the above reasons, it is desirable to achieve a nitride formation without using an oxide intermediate. Hector *et al.* developed a nitride sol-gel process which employs metal dialkylamides $M(NMe_2)_n$ as nitride precursors.[7] By operating in air-free conditions, they were able to eliminate oxygen contamination in the synthesis. Specifically for TiN, the transamination of $Ti(NMe_2)_4$ with primary amines results in primary amide groups which can self-condense and form alkylimide bridges. By annealing of this dip-coated sol-gel film under ammonia, a nanocrystalline TiN film was obtained.[8] In their later work, they applied this method in synthesizing macroporous TiN by polystyrene template infiltration.[9] They also showed that the attempt to convert macroporous TiO_2 led to collapse of the pores. Despite the success of this method, extensive efforts are required for handling very air-sensitive precursors. In fact, Kaskel *et al.* demonstrated a facile approach in synthesizing high surface area titanium nitride by ammonolysis of $TiCl_4$ complexes.[10] This inspired our study of using metal chlorides as starting precursors to synthesize templated morphologies.

Recently, a chromium nitride (CrN) supported platinum catalyst was reported to possess higher electrocatalytic activity and stability than Pt/C for both oxygen reduction reaction (ORR) and methanol electrooxidation for PEMFC applications.[11, 12] Herein, we focus on a synthetic method to produce an ordered macroporous chromium nitride (CrN) and chromium titanium nitride from metal chloride complexes. The sol-gel process by ligand exchange from an external nitrogen source turned out to be not necessary for the network formation. This method was proven to be a facile method to produce ordered porous metal nitrides, and can be effectively extended to fabricate mixed metal nitrides.

4.2 Macroporous chromium nitride (CrN)

Polystyrene (PS) beads were used as template and metal chloride complexes were used as metal precursors in the synthesis of macroporous CrN. Carboxylate-functionalized polystyrene (PS) beads (500-nm-radius) in a 2.7 vol.% aqueous suspension was mixed with ethylene glycol and water in a volume ratio of 1: 0.4: 6. The mixed solution was sonicated for 10 minutes before dropping on a polystyrene Petri dish followed by drying on a hot plate at 50°C for 48 hours. The solution was completely dry after this process. The product is a white film, which is scraped off and weighed. 0.0343g $CrCl_3{\cdot}6H_2O$ was completely dissolved in 10 mL of ethanol and was mixed with 0.0200g of the scraped polystyrene. The mixture was dried in a glass Petri dish on top of a hot plate of 50°C for 12 h. Then the dried product is scraped and put into an alumina boat for annealing. The boat is placed in a silica tube with airtight, stainless steel end-caps with valves on input and output gas lines. All gases were purified to remove oxygen or water using pellets of copper, nickel, palladium and platinum on zeolite supports. The silica tube was placed in a split tube furnace for annealing. The chromium precursor infiltrated PS array was heated under flowing ammonia to 450°C using a ramp rate of 50°C/hour. The product was kept at 450°C for 6 hours before a controlled cooling (100°C/h) to room temperature. Due to the tendency to form a surface oxide upon exposure to air, all samples were carefully handled and let slowly exposed to air after annealing to minimize the extent of oxide formation. This synthesis method is schematically shown in Figure 4.1.

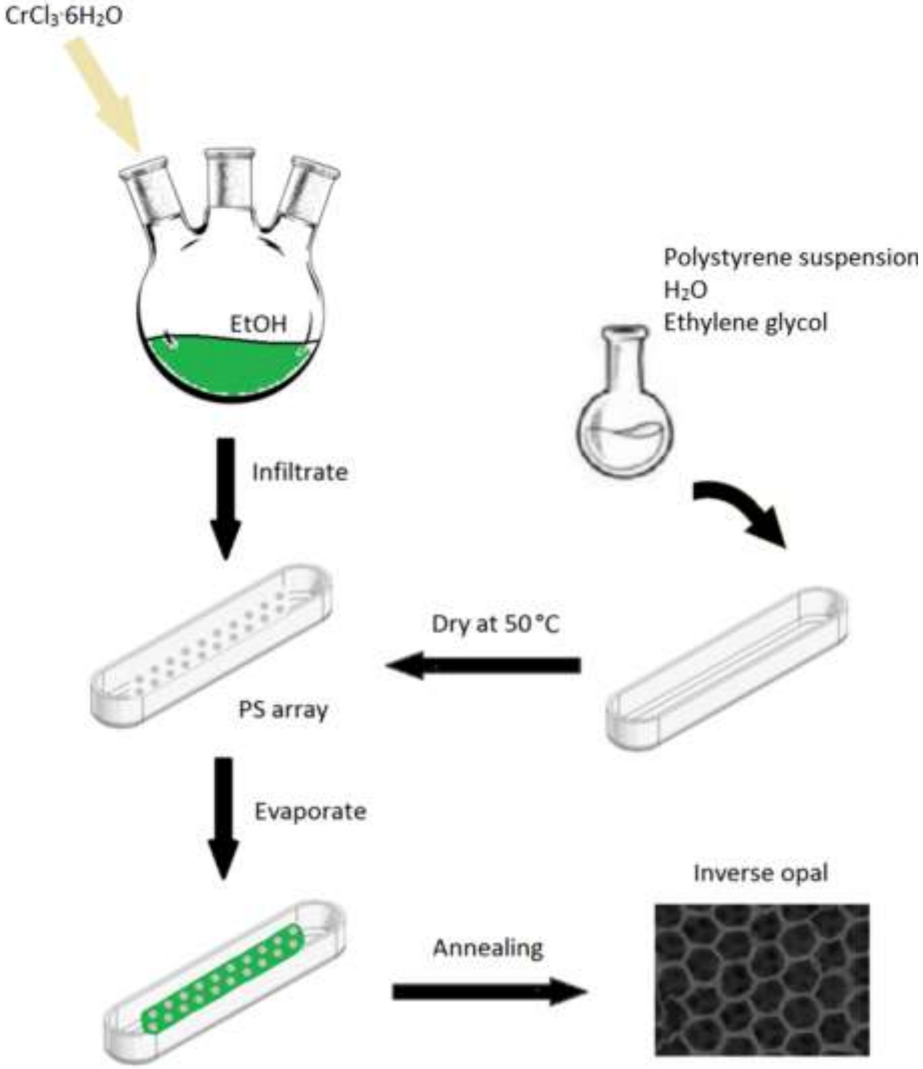

Figure 4.1. Synthesis method for macroporous transition metal nitride.

Several samples were prepared by the same experimental procedure and the results were similar for all. The powder X-ray diffraction pattern for CrN nanoparticles (Figure 4.2) can be indexed with the expected face-centered cubic phase of bulk chromium nitride. The blue lines are the peak positions of pure CrN with lattice parameter of 4.140 Å (PDF No. 04-007-9961). The formation of an oxynitride or carbonitride, as well as defects due to nitrogen vacancies $MN_x\square_{1-x}$, will cause a shift in the lattice parameters and the resulting peak positions. Carbonitride formation from solid state synthesis typically requires high temperature (above 800°C) and is unlikely to happen at 450°C.[13] Defect structure and oxynitride formation decrease the lattice constant and will shift the peak position to the higher angles. Experimental peaks shown in Figure 4.2 match well with the standard peak position, indicating low oxygen content and few defects in the structure. The peaks are very broad and have narrow tips. This indicates nanoscale crystallite domains with a relatively broad distribution of domain sizes. The average CrN crystallite domain size is calculated to be 4.7 ± 0.8 nm using Halder-Wagner method. The lattice parameter was calculated to be a = 4.138 (12) Å using whole powder pattern fitting (WPPF) technique, giving a value which is very close to the reference data of 4.140 Å.

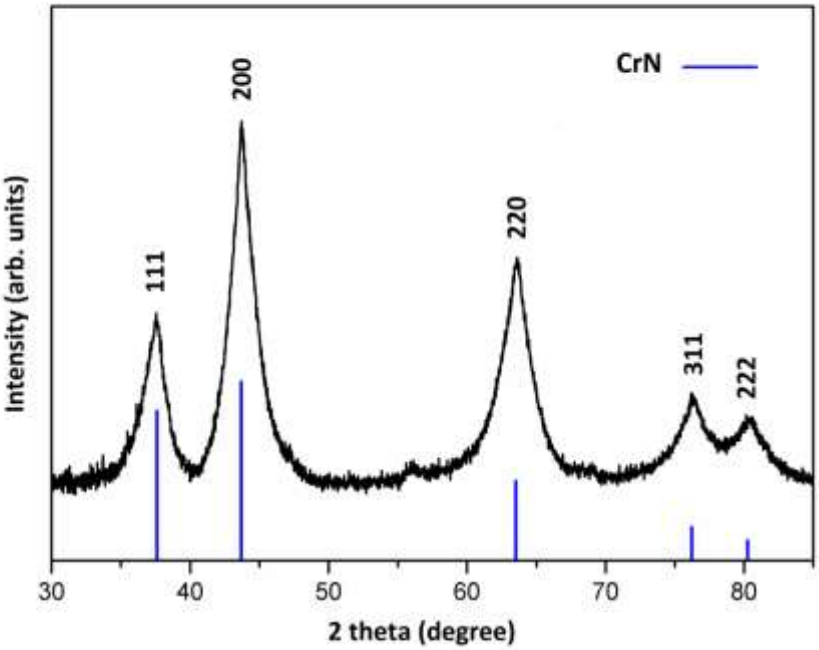

Figure 4.2. XRD pattern of macroporous CrN.

Figure 4.3 is a SEM image showing the morphology of the macroporous CrN. As is seen in the lower inset, the pores are interconnected. This important feature of the products allows effective flow of gases or liquids during operation. Some surface inhomogeneities are also present; this is possibly due to residual precursor on the surface of the sample made by infiltration.

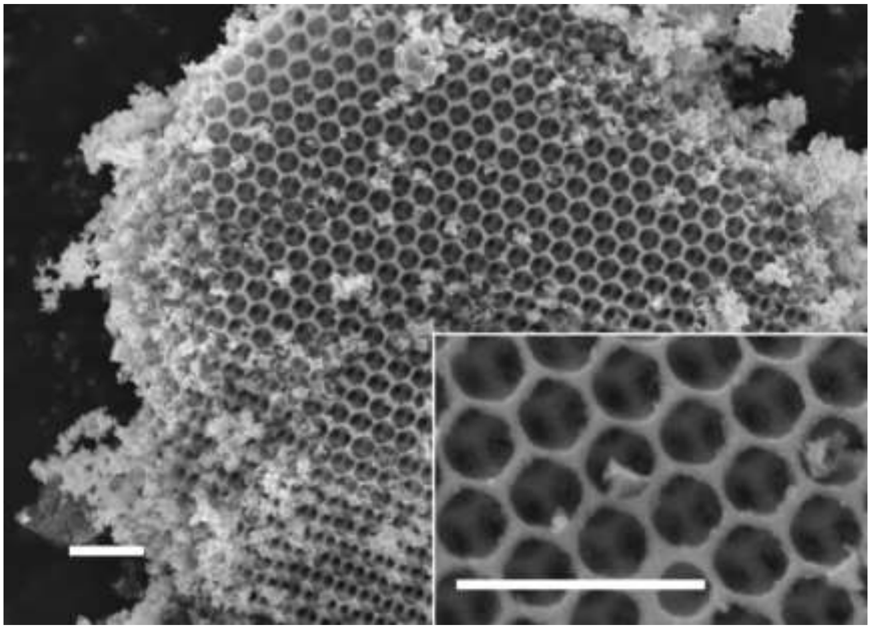

Figure 4.3. SEM image of as-made macroporous CrN, the lower right inset is a detailed look into the macroporous structure. Scale bars are 1 micron.

HRTEM images were taken to show the crystalline nature of the walls of the macroporous structure. Multiple lattice fringes, as shown in Figure 4.4, were observed at the edge of the wall. This confirmed the crystallinity and small domain sizes of macroporous CrN. A distribution of domain sizes, previously proposed from the XRD pattern, can also be confirmed by the TEM image.

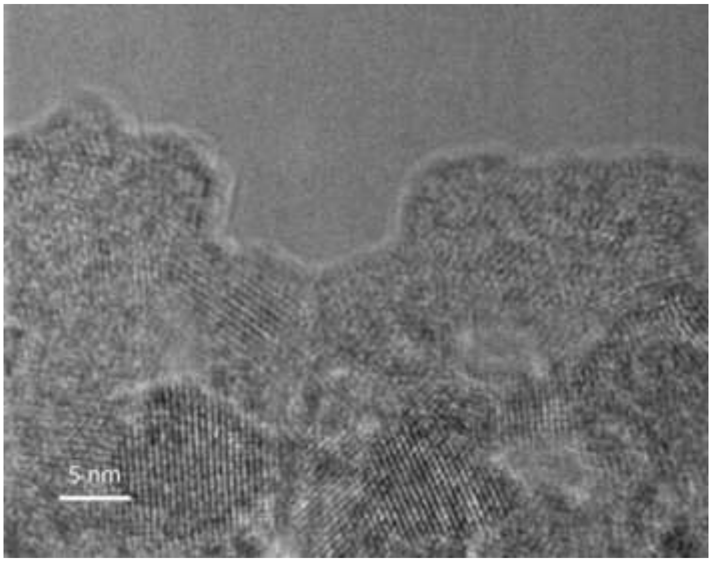

Figure 4.4. Bright field HRTEM image of macroporous CrN.

TGA was carried out in air to determine the carbon content in the sample from PS beads. The change of weight and its derivative as a function of time is shown in Figure 4.5. The temperature profile is shown by dashed line. Due to the release of species absorbed in air, such as water, a mass decrease before 120°C is observed in the raw data. The sample weight at 120°C is set as reference weight and Figure 4.5 only shows data after 120°C. Two stages of weight increase as well as a drop of weight can be observed from the image. The drop of weight is probably due to the oxidation of residual carbon in the sample, and the increase of weight is due to the oxidation of chromium nitride (CrN) to chromium oxide (Cr_2O_3). The product of Cr_2O_3 is confirmed by XRD. From the DTA curve, it can be concluded that the carbon oxidation starts near 400°C and is completed near 480°C. In contrast, the oxidation of the CrN begins at a lower temperature (about 120°C) but is nearly complete only after 90 minutes at 550°C. The loss in weight from the peak at ~410°C to the minimum at ~480°C is 5.2% of the material weight (reference weight at 120°C). Since the weight is also constantly increasing due to oxidation of CrN, this provides only a rough estimate of the carbon content in the material. The real carbon content should be a little higher than this estimate. A method of estimating the maximum carbon content is to assume that the sample was completed converted to Cr_2O_3 from CrN. By this calculation, the result indicates 90.5% of material is CrN, giving a carbon content of 9.5%. This may be a slight overestimate, since the derivative of the weight is still slightly above zero at the end. Besides, despite the identified single phase of Cr_2O_3 in the XRD pattern in Figure 4.6, complete exclusion of nitrogen in the crystal lattice from annealing in air is not certain. An EDX study of the heated sample also reveals a nitrogen content of about 6%, also shown in Figure 4.6. Using these estimates, the carbon content in the macroporous CrN is determined to be between 5 ~ 10 wt.%.

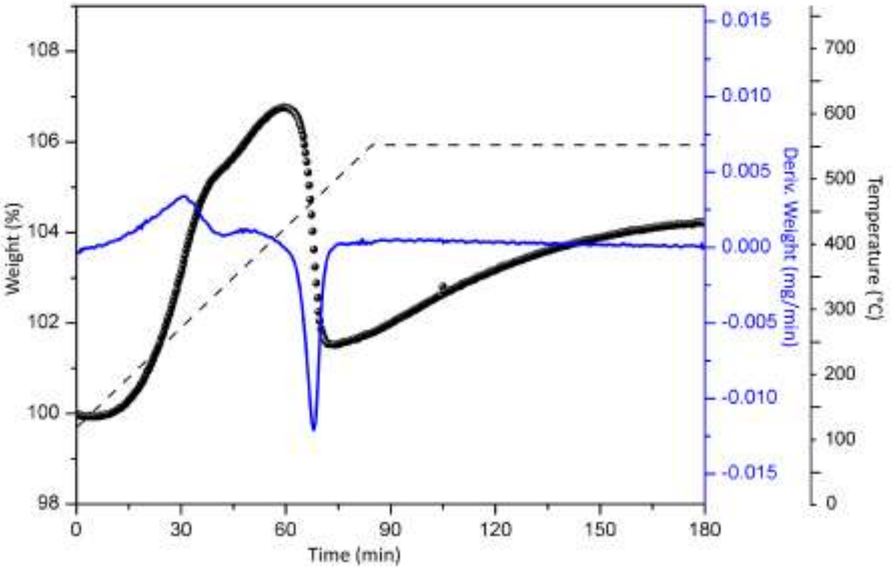

Figure 4.5. TGA thermogram of macroporous CrN. Black dots are the measured data of sample weight; the continuous blue line indicates the derivative of the weight. The temperature profile is given in the dashed line.

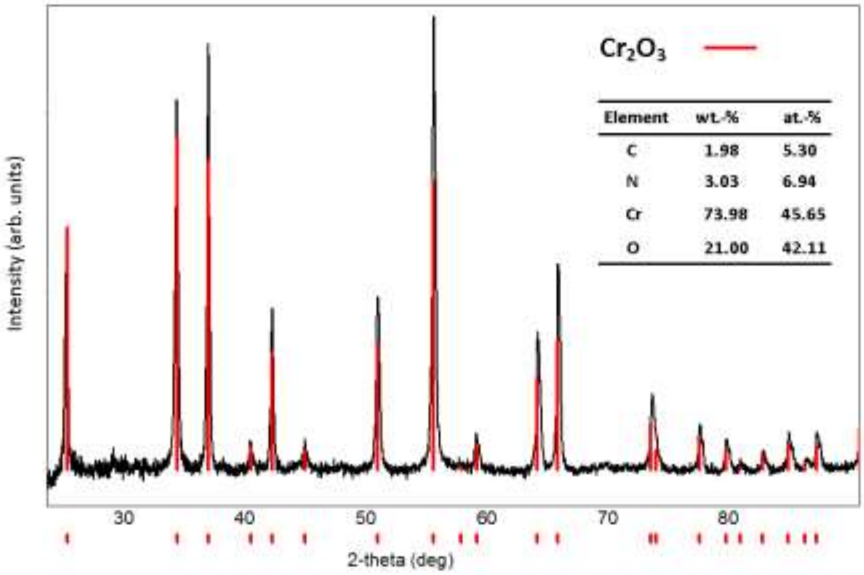

Element	wt.-%	at.-%
C	1.98	5.30
N	3.03	6.94
Cr	73.98	45.65
O	21.00	42.11

Figure 4.6. XRD diffraction pattern of macroporous CrN after TGA, indicating a pure Cr_2O_3 phase. The inset is an elemental composition from EDX.

The surface chemical states of the sample was probed using XPS. Survey scans and high-resolution scans were conducted. Elemental composition was determined from peak area calculations and is listed in Table 4.1.

Table 4.1. Elemental content determined by XPS.

Element	Pos./ Binding Energy (eV)	Atomic %
C 1s	258.0	27.40
O 1s	530.0	26.34
Cr 2p	575.0	21.66
Cl 2p	198.0	1.30
N 1s	396.0	23.31

The usage of sticky carbon film for loading the sample in XPS measurements makes it difficult to determine the carbon and oxygen content from the XPS data. A small amount of residual chlorine is detected. The chromium nitrogen ratio was determined to be very close to 1:1. High-resolution XPS scans for N(1s) and Cr(2p) are shown in Figure 4.7.

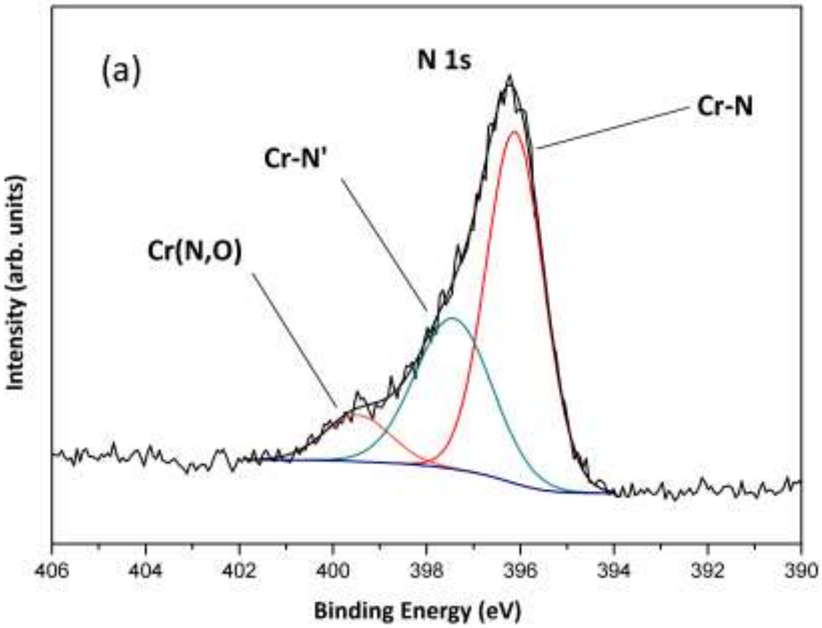

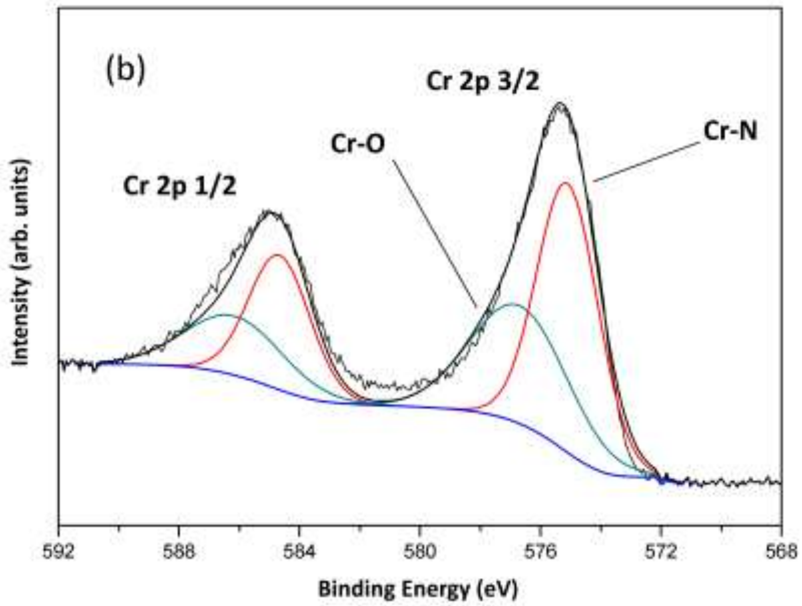

Figure 4.7. The profile of N 1s region (a) and Cr 2p region (b) from XPS high-resolution measurement. The black lines are the fitting curve and the blue lines are the background.

The nitride sample is conductive so the data is not calibrated by the standard carbon peak position.[16] When fitting the curve by setting constraints on the peak position using reported values, the measured data can't be perfectly matched. This might due to complex environment around the atom, such as possible N-Cr-O bonding in an oxynitride, so the measured data is deconvoluted and peaks are assigned to different chemical states according to reference data. The Cr 2p 1/2 was also used in peak deconvolution. A peak area ratio of 2:1 for Cr 2p 3/2 to Cr 2p 1/2 and same value of Full Width at Half Maximum (FWHM) were used as constraints during the deconvolution of the peaks. Different values for spin-orbit splitting were reported such as 9.20 eV (Cr) and 9.8 eV (Cr_2O_3), but the value for bulk CrN is not known. Thus the constraint on the energy difference between 2p 3/2 and 2p 1/2 peak positions is not set, but the results always fall into the region of 9.5 ± 1 eV.[15]

In the N 1s spectrum, major components of the peaks are contributed by the Cr-N bonds (396.1 eV, 397.4 eV) and perhaps a low level of oxynitride (399.5 eV). The two different states for CrN could be explained by oxygen impurities or defects in the structure. The possible oxynitride peak is very small. From the Cr 2p profile, two peaks at the position of 575.1eV and 576.7 eV are found. The previous one can be assigned to CrN (575.8 eV) and the later one falls into the region of CrO_x (576.3 – 579.8 eV).[15] The formation of a surface oxide layer is likely to occur upon air exposure for nitride materials, particularly for a nanocrystalline nitride with a higher reactivity.

4.3 Macroporous chromium titanium nitride ($Cr_{0.5}Ti_{0.5}N$)

Ternary/mixed metal nitrides are generally difficult to make due to differences in activities and properties of the two different metal precursors. Here we report efforts to expand this method to make mixed metal nitrides. Specifically, we set out to prepare free-standing, macroporous $Cr_{0.5}Ti_{0.5}N$. The procedure to prepare the mixed metal nitride is similar as for CrN. Half the amount of the chromium precursor was used, with the addition of equivalent amount (molar ratio) of $TiCl_4 \cdot 2THF$. During the heating stage, the infiltrated PS array was heated to 450°C and kept for 3 h before raising the temperature to 550°C. The product was held at 550°C for 24 h and then cooled. The same heating and cooling rates as for the CrN sample were used.

Figure 4.8 shows the powder X-ray diffraction pattern of macroporous $Cr_{0.5}Ti_{0.5}N$. The peaks can be indexed on a single face-centered cubic cell. The broad peaks indicate a small average domain size, which is calculated to be 4.0 ± 0.7 nm. The marked peaks are due to background peaks from the sample holder.

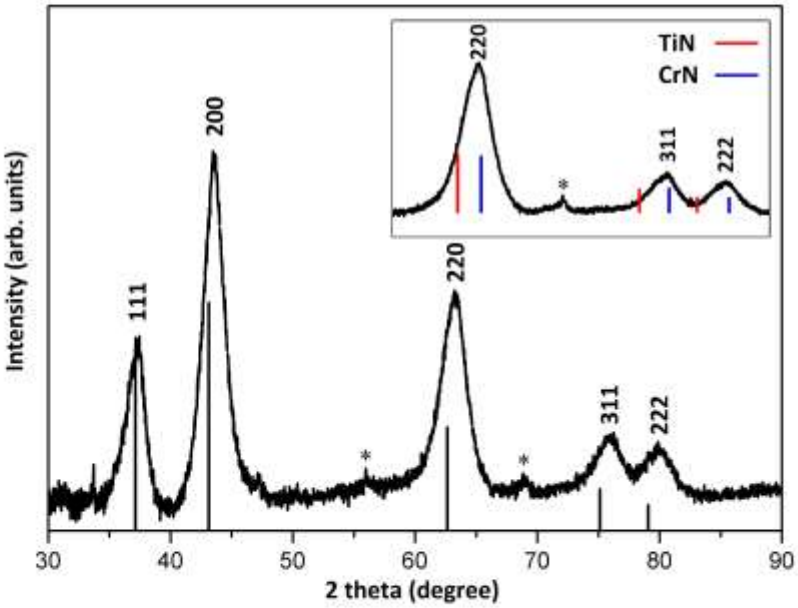

Figure 4.8. XRD pattern of macroporous $Cr_{0.5}Ti_{0.5}N$ product.

The black line corresponds to a reported PDF card of a face-centered cubic $Cr_{0.5}Ti_{0.5}N$ with a lattice parameter of 4.192 Å (PDF no. 04-016-6620). The reported data also matches the expected value of 4.188 Å, assuming the lattice parameter of a $Cr_{0.5}Ti_{0.5}N$ solid solution follows Vegard's law, and thus is adopted for the reference value. By Whole Powder Pattern Fitting (WPPF), the lattice parameter was calculated to be a = 4.1569 (10) Å. A shift in peak positions from the PDF data, which is more obvious at higher angle, is observed in the figure. As discussed previously, factors such as the possible formation of oxynitride or the presence of nitrogen vacancies could result in such shift of the peak positions. The titanium precursor used in the preparation is air-sensitive and might react with water upon exposure to air. An air-free technique is not used for the preparation and may result in oxynitride formation. The cause of the shift in peak positions is investigated in more detail in later discussions.

Another question here is whether the product is a $Cr_{0.5}Ti_{0.5}N$ solid solution, or a mechanical mixture of CrN and TiN. Since the lattice parameters of CrN and TiN are very close, lower-angle peaks are not sufficient to distinguish a single-phase product with a mixture that shows only one peak but contains two distinct peaks that are very close to each other. To prove the product is a solid solution, repeated measurements were conducted on higher-angle peaks. The inset in Figure 4.8 shows the (220), (311) and (222) peaks, and the peak position for CrN and TiN. The difference in the peak position from those expected for CrN and TiN is obvious at high angles. Since the line width is on the order of the difference between the bulk TiN and CrN peak position, a mixture of two products will result in a peak with a nearly flat top, which is not seen in measured pattern. This suggests that the product is not a mixture of CrN and TiN. However, oxide impurities or nitrogen vacancies in TiN might be present, which would lead to higher angle peak positions. So we still can’t completely rule out the possibility of forming a mixture of $TiN_{1-x}O_x$ and CrN in the product.

The inverse opal morphology of the $Cr_{0.5}Ti_{0.5}N$ product is confirmed by SEM, as shown in Figure 4.9.

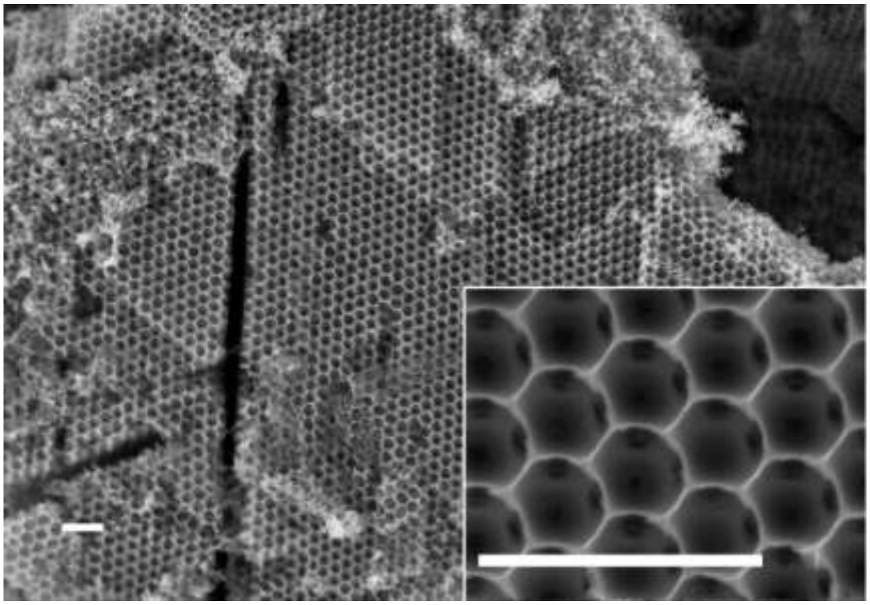

Figure 4.9. SEM image of $Cr_{0.5}Ti_{0.5}N$. Scale bars are 1 micron.

An EDX study of elemental distribution was carried out using STEM. Figure 4.10 (a) is a High-Angle Angular Dark Field (HAADF) image of the macroporous $Cr_{0.5}Ti_{0.5}N$. A line scan was conducted and the path is shown as the yellow line in the figure. Concentrations of Cr and Ti are shown in Figure 4.10 (b). It was observed that the elemental concentration corresponds well with the thickness of the wall, and the Cr Ti ratio is constant throughout this path, despite some possible instrumental errors. With a resolution of a few nanometers, these results show that chromium and titanium are reasonably well mixed. This is a further evidence for the formation of a CrN-TiN solid solution ($Cr_{0.5}Ti_{0.5}N$).

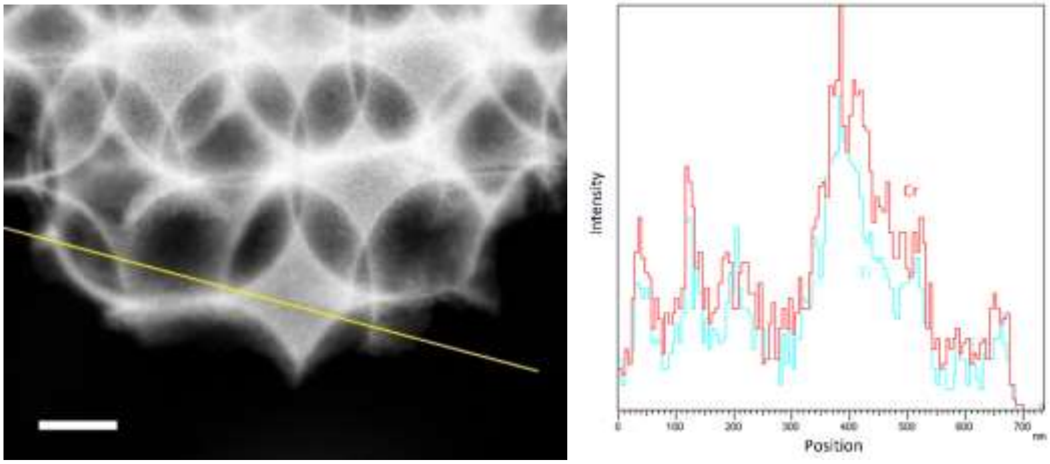

Figure 4.10. (a) HAADF image of macroporous $Cr_{0.5}Ti_{0.5}N$. The yellow line indicates the path of the EDX line analysis. Scale bar is 100 nm. (b) Elemental concentration of Cr and Ti vs. position.

A thermogravimetric study was carried out to determine the amount of carbon residue, and to provide some information on materials composition. The result is shown in Figure 4.11.

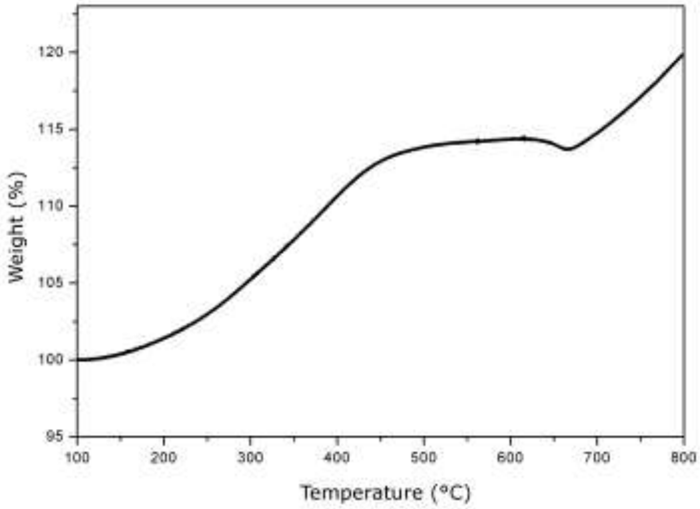

Figure 4.11. TGA thermogram of $Cr_{0.5}Ti_{0.5}N$ under air. Temperature was ramped to 800°C using a ramp rate of 5°C/min.

A plateau from ~450°C to 600°C followed by a slight decrease in weight is observed, both are attributed to the oxidation of carbon. Above 600°C, the weight exhibits steady increase up to 800°C. The continuous oxidation of the nitride overlaps with the oxidation of carbon which leads to a flat region, making it difficult to accurately determine the amount of carbon. The overall increase in weight is calculated to be 19.7%, smaller than the theoretical value of 21.9%, assuming $Cr_{0.5}Ti_{0.5}N$ is completely converted to TiO_2 and Cr_2O_3. With the derivative of the mass at 800°C being very positive, the actual increase in weight might exceed the theoretical maximum value. This cannot be attributed to the presence of oxynitride, but might be explained by nitrogen vacancies initially present or the trapping of nitrogen in the lattice during oxidation.

Table 4.2 is the elemental composition of $Cr_{0.5}Ti_{0.5}N$ heated under NH_3 to 550°C calculated by XPS. As can be seen, Cl is no longer present in the material, possibly due to a higher annealing temperature. Cr, Ti, N ratio is found to be 1:1.00:2.07, which is very close to the expected stoichiometry of $Cr_{0.5}Ti_{0.5}N$.

Table 4.2. Elemental composition determined by XPS.

Element	**Pos./ Binding Energy**	**Atomic%**
C 1s	258.0	18.96
O 1s	530.0	32.41
Cr 2p	575.0	11.95
Ti 2p	457.0	11.98
N 1s	396.0	24.70

Figure 4.12 shows the high-resolution analysis over Cr 2p and Ti 2p regions. Peak deconvolution gives two peaks for chromium, similar to the previous CrN sample. For titanium, two peaks at 456.0 eV and 457.5 eV were identified. The first one can be assigned to TiN, but the second peak can't be assigned according to reported values: Ti (453.7 – 454.1 eV), TiO (455.1 ± 0.2 eV), TiN (455.8 ± 0.2 eV), TiO_2 (459.2 - 458.7 eV). This peak falls in the region between TiN and TiO_2 and is hypothesized to be an oxynitride peak from a titanium atom connected to both a nitrogen atom and an oxygen atom.

The results indicate that at the particle surface (first few nm), chromium mainly exists as CrN and titanium is mostly in the form of oxynitride. This result is expected considering the nano-scale particles and the surface sensitive techniques used. It is also known that titanium is more oxyphilic compared to chromium.

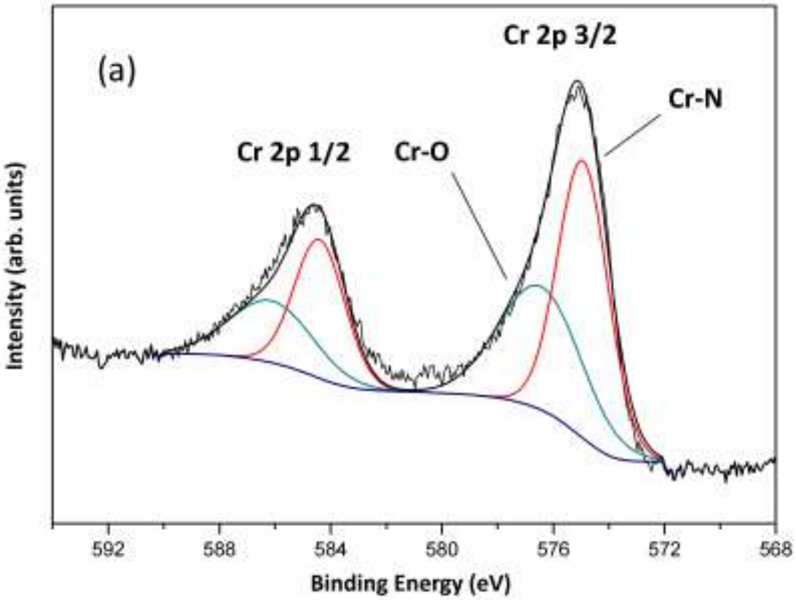

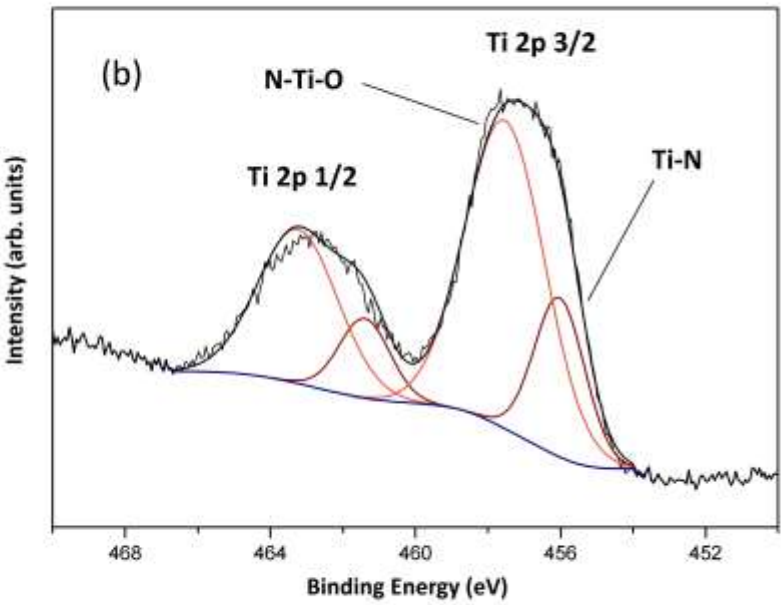

Figure 4.12. a) Cr 2p profile of macroporous $Cr_{0.5}Ti_{0.5}N$ measured in XPS. b) Ti 2p profile of macroporous $Cr_{0.5}Ti_{0.5}N$.

The focus of this work is to explore a synthetic method for obtaining nanocrystalline ordered porous metal nitride, or more importantly, a mixed metal nitride, which is typically difficult for other existing methods, rather than the materials properties. As a reference, reported data for electrical conductivity of bulk CrN is 1.1×10^3 S/cm, much higher than the carbon-based supports (~4S/cm).[16, 17] In a typical experiment setup, for nanocrystalline nitrides, or the macroporous nitrides, it is expected that the measured data is lower than the reported data for bulk materials due to weak particle-particle contacts and/or the porosity of the sample.

Besides a high conductivity, the nano-scale particles from the low-temperature synthesis possess high surface area, making them ideal candidates as catalyst supports. BET data was previously reported using a similar synthetic technique. TiN made from ammonolysis of $TiCl_4{\cdot}2THF$ for one hour at 600°C and 700°C was reported to have a surface area of 230 m^2/g and 212 m^2/g, respectively.[10] For the samples CrN and $Cr_{0.5}Ti_{0.5}N$ prepared in the same method, but without the PS template, the measured data for the surface area is 99.2 m^2/g for CrN and 103.8 m^2/g for $Cr_{0.5}Ti_{0.5}N$. The measured surface area of commercial carbon black (Vulcan XC72R) is 265.4 m^2/g.

4.4 Interconversion of CrN and Cr_2O_3

A possible conversion from macroporous CrN to Cr_2O_3 and then back to CrN was attempted. This effort was a test on the thermal stability of porous network during high temperature oxidation/nitridation. A similar interconversion of a Ti/W oxide and nitride was previously reported in our group.[18] For CrN, previous work reported that a nitridation for 8 h at 800°C completely eliminated the oxide phase.[4] It should be pointed out that the conversion temperature is dependent on oxide crystal size and any residual template materials in the sample. In fact, experiments in our lab showed a complete conversion to CrN with 6 hour ammonolysis at 650°C, from a macroporous Cr_2O_3 with a calculated crystal domain size of 24.9 ± 1.0 nm.

The procedures for interconversion is to heat the macroporous CrN made from previous synthesis under flowing air to 550°C for 1 hour using a ramp rate of 300°C/hour, followed by a controlled cooling to room temperature in about 2 h. To convert the annealed sample back to the nitride, samples were divided into several groups and heated in flowing ammonia at 650°C and 700°C for 6 hours, respectively, with a ramp rate of 100°C/h and a cooling rate of 200°C/h.

Figure 4.13 (a) shows the XRD patterns of all samples with calculated domain size. Both converted materials showed a rock salt structure expected for CrN. However, data for the sample converted at 600°C, which is not shown here, showed the presence of remaining Cr_2O_3. Figure 4.13 (b) is a SEM image of the initial Cr_2O_3 sample made by oxidation of macroporous CrN in air at 550°C. While the general porous morphology is preserved, the details were mostly lost. A noticeable growth in particle size is also observed. Figure 4.13 (c) and (d) are SEM images of the oxides that were re-nitrided by ammonolysis at 650°C and 700°C, respectively. The sample heated at 650°C exhibits an inverse opal morphology, while the sample heated at 700°C has mostly lost its original morphology. The pores within the sample provides open space for oxide growth, this might help maintain the porosity during conversion.

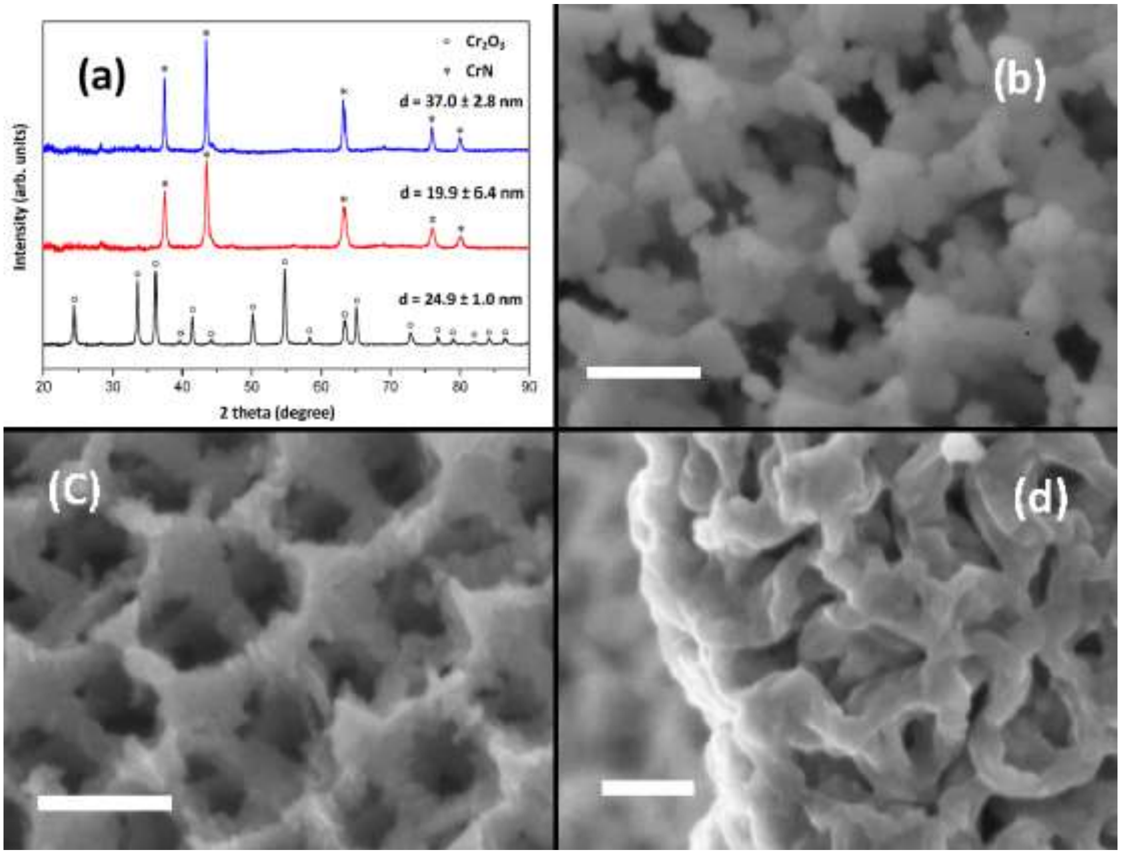

Figure 4.13. (a) XRD patterns and calculated domain sizes of the initial macroporous Cr_2O_3 (black) and CrN obtained from ammonolysis at 650°C (red) or 700°C (blue). (b) Macroporous Cr_2O_3 made from as-made macroporous CrN. (c) CrN obtained from Cr_2O_3 heated in 650°C. (d) CrN obtained from Cr_2O_3 heated in 700°C. All scale bars are 200 nm.

In our work, the conversion from macroporous oxide to nitride succeeded while preserving the porous morphology. However, the calculated domain size of CrN grows to 20 nm compared to as-made CrN (5 nm), and the temperature window for successful conversion is very narrow (between 600°C – 700°C). In contrast, a direct nitride formation which produces smaller particles and is not restricted by nitridation temperature thus shows superiority. Particularly, this method possesses great potential in producing mixed metal nitrides in any stoichiometric ratio, which is difficult for the common oxide route. More discussion about this method is presented below.

4.5 Discussions

4.5.1 Formation of a porous crystalline phase

The formation of a crystalline nitride from oxide typically requires high temperature processing (above 600°C).[5, 6] From chloride precursors, we observed lower temperature access to crystalline nitride phases with the XRD pattern of face-centered cubic CrN appearing even after annealing in flowing ammonia at 350°C for 3 hours, as shown in Figure 4.14. This feature is important to obtain a crystalline phase before the decomposition of templates at higher temperatures. At the same time, compared to metal oxides with high sinterability, crystals of metal nitrides grow slowly, which enables better preservation of the inverse opal morphology. In this work, experiments were also conducted trying to obtain macroporous Cr_2O_3 directly from a PS bead template. Although we lowered the temperature to 400°C (the decomposition of PS is found to be between 300°C and 400°C as shown in Figure 4.15) and annealing time to 1.5 h, we were still not able to obtain good morphology due to large crystallite growth (calculated domain size ~ 30 nm). A typical SEM image of the samples obtained from this method is shown in Figure 4.16. It can be easily observed that the porous morphology was very poor. This is a major reason that many reports of producing macroporous oxides involve the use of hard templates to suppress the crystal growth.

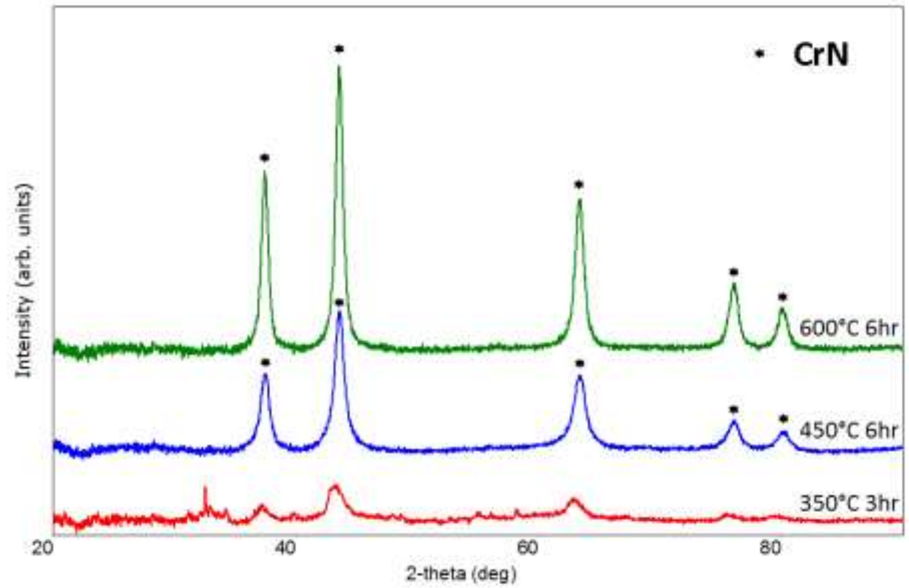

Figure 4.14. XRD patterns of samples made by ammonolysis of $CrCl_3{\cdot}6H_2O$ precursor under different conditions. The crystal domain sizes for 450°C and 600°C samples were calculated to be 9.0 nm and 11.7 nm, respectively.

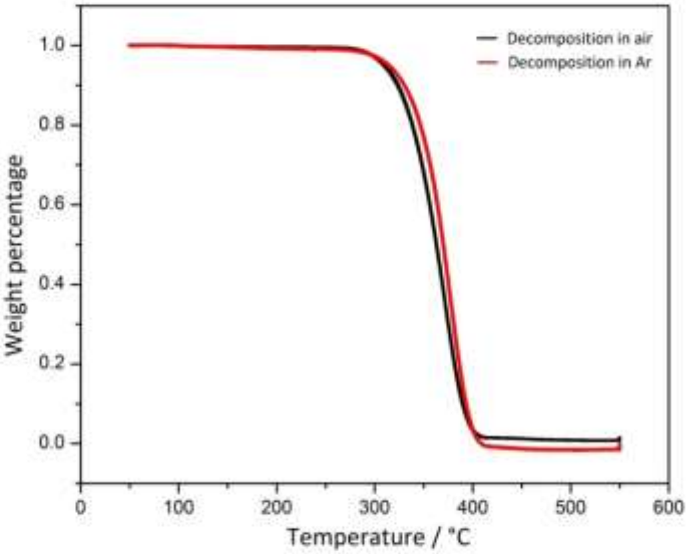

Figure 4.15. TGA curve of polystyrene (PS) beads decomposed in air (black line) and in Ar (red line).

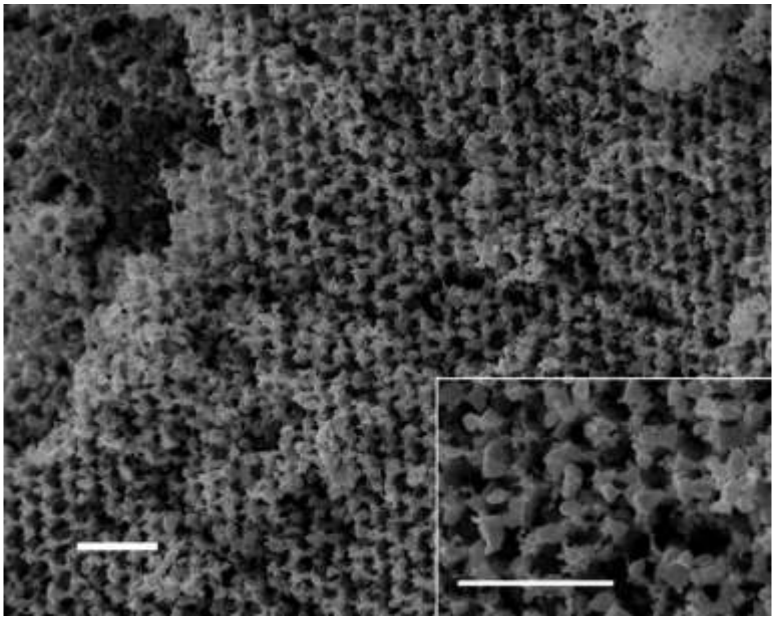

Figure 4.16. SEM image of Cr_2O_3 produced by annealing an oxide sol infiltrated into a PS array in air. The domain size is calculated to be 35 nm. All scale bars are 1 micron.

4.5.2 Possible oxygen content in Cr-Ti-N

In the synthesis of mixed metal nitride $Cr_{0.5}Ti_{0.5}N$, air-sensitive $TiCl_4$·2THF was dissolved in ethanol and was not given extra effort to prevent its contact with the air. The XRD pattern of the product shows a slight peak position shifting with regard to the reference data. Despite the shifting in XRD pattern, the XPS data showed the atomic percentage of Ti, Cr and N to be roughly 1:1:2 (Table 4.2). To investigate the cause of peak position shifting, we synthesized $Cr_{0.5}Ti_{0.5}N$ nanoparticles without templates using different annealing temperatures and characterized them using XRD and a combustion analysis method, which can more accurately determine the oxygen and nitrogen content in the sample. Two samples were prepared: the first was annealed at 550°C under flowing ammonia for 24 h (Cr-Ti-N:A) and the second at 800°C under ammonia for 6 h (Cr-Ti-N:B). The results are shown in Figure 4.17.

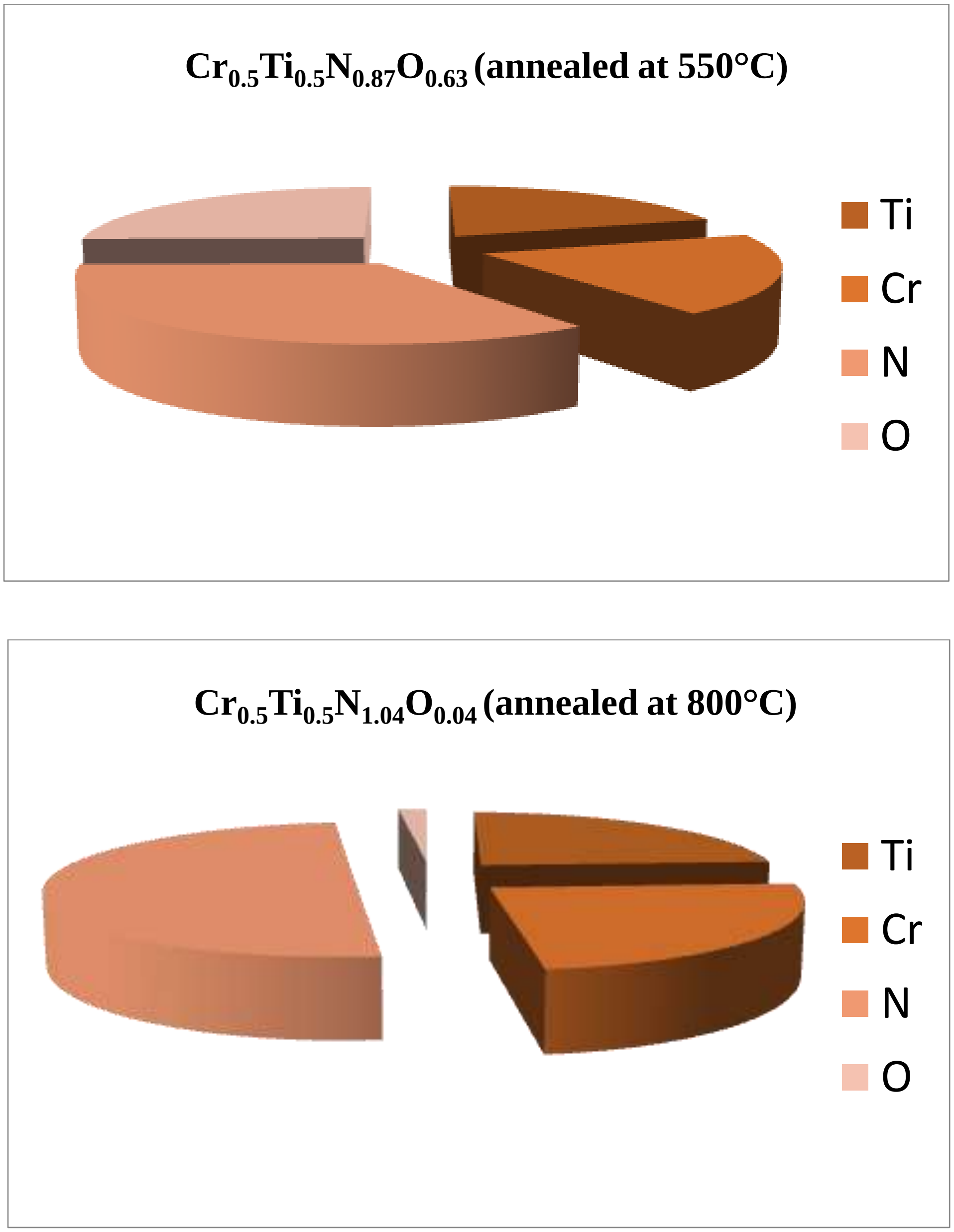

$Cr_{0.5}Ti_{0.5}N_{0.87}O_{0.63}$ (annealed at 550°C)

$Cr_{0.5}Ti_{0.5}N_{1.04}O_{0.04}$ (annealed at 800°C)

Figure 4.17. Results of composition analysis for $Cr_{0.5}Ti_{0.5}N$ prepared using different ammonolysis temperatures.

The data shows that the sample annealed at 800°C is mostly nitride (Ti:Cr:N:O = 1:1:2.08:0.08), while the sample annealed at 550°C has considerable amount of oxygen impurities. In this case, the shift in the peak position is likely due to the oxygen content. However, this experiment cannot determine the exact cause for the peak shifting for the porous sample, which was shown in XPS to have a metal nitrogen ratio that matches the theoretical values expected for the nitride. Other factors such as vacancies in lattice could also result in peak position changes.

4.5.3 Formation of solid solution Cr-Ti-N

In the previous section, the XRD pattern of $Cr_{0.5}Ti_{0.5}N$ and high-resolution EDX line analysis in the STEM indicated the possible formation of a solid solution. Thus it is interesting to look at the conversion between the $Cr_{0.5}Ti_{0.5}N$ with its corresponding oxide. Figure 4.18 shows the phase diagram of Cr_2O_3-TiO_2.

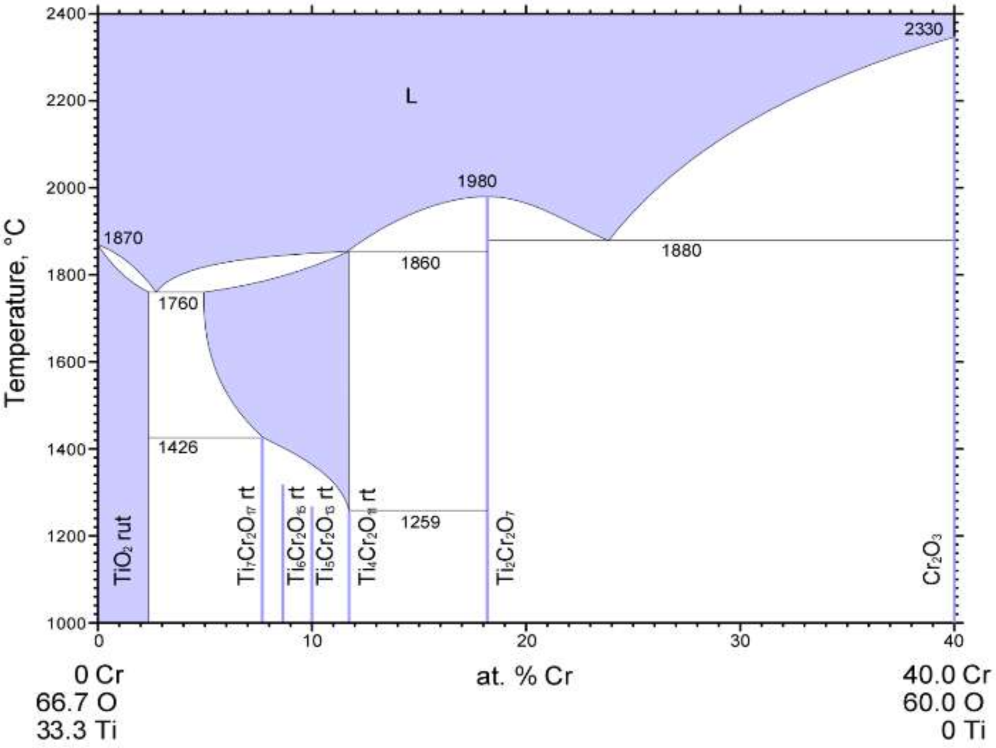

Figure 4.18 Phase diagram of Cr_2O_3-TiO_2.

A $Ti_2Cr_2O_7$ phase with Ti and Cr ratio of 1 to 1 can be found in the phase diagram. However, besides $Ti_2Cr_2O_7$, other Ti-Cr-O phases with a Ti to Cr ratio of 1:1 also exist, which do not show up in this phase diagram where the valence number of Cr and Ti are fixed to be Ti^{+4} and Cr^{+3}. It is expected that upon heating in air, a solid solution of CrN and TiN with atomically mixed Cr and Ti will be converted directly to Ti-Cr-O, which keeps the same Cr to Ti ratio. However, after heating the samples that was made without template in air at 900°C and further at 1100°C, none of the expected products were detected using XRD. Peaks in the XRD pattern (Figure 4.19) can be partly assigned to Cr_2O_3 and TiO_2 with many peaks remaining unidentified. The crystal domain size of chromium oxide and titanium oxide are calculated to be within 30 – 80 nm. This data suggests that the originally mixed Cr and Ti atoms will have to diffuse through this distance to separate from each other to form a single crystalline domains with only Cr/O or Ti/O atoms. This behavior is unexpected for our samples in which the Cr and Ti atoms were determined by multiple high-resolution EDX analysis to be mixed at least within a few nanometers, if not a classic solid solution. Since we used the samples without the pores, it is possible that the porosity could play a role. But it is also possible that due to the difference in bonding strength with oxygen, different elements can behave differently upon heating in air.

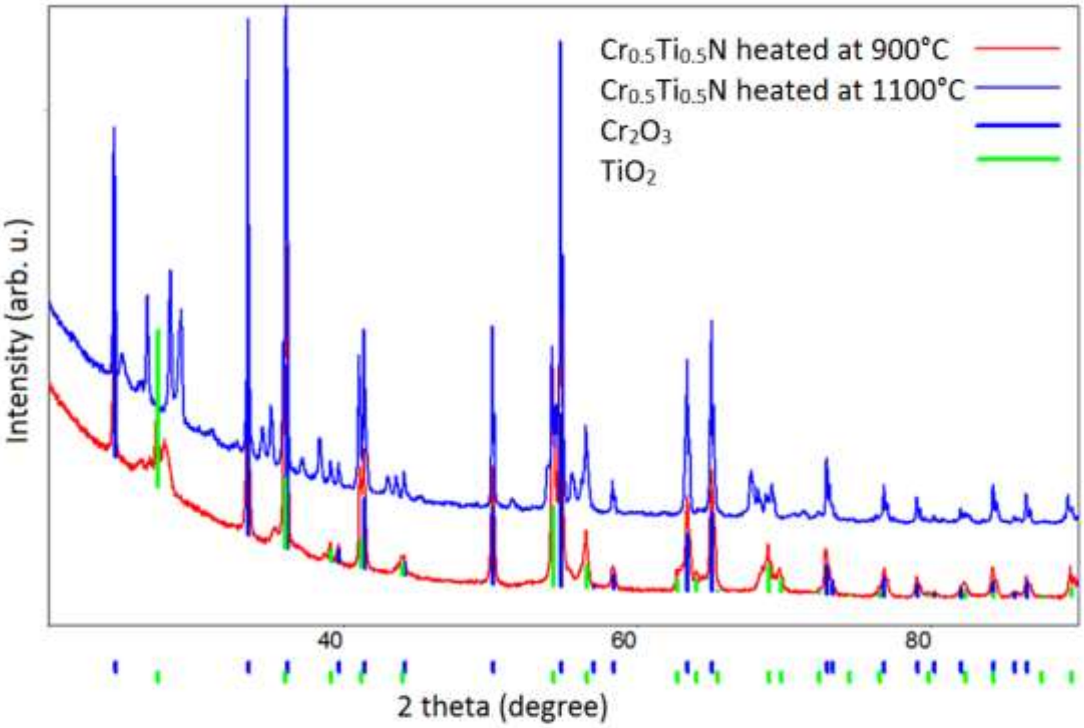

Figure 4.19. XRD pattern of $Cr_{0.5}Ti_{0.5}N$ annealed in air at 900°C and again 1100°C.

4.6 Conclusions

Syntheses of macroporous CrN and $Cr_{0.5}Ti_{0.5}N$ from metal chloride complexes were demonstrated. The CrN product is a crystalline macroporous material with a crystal domain size of about 5 nm. A small amount of carbon (5% - 10 wt. %) is estimated to exist in the final product. The chemical state of chromium was shown to be mostly chromium nitride with small amount of chromium oxide by XPS.

This synthetic method is also shown to be applicable in making macroporous mixed metal nitride $Cr_{0.5}Ti_{0.5}N$. A single phase, face-centered cubic structure chromium titanium nitride was obtained. The product is hypothesized to be a solid solution, instead of a mechanical mixture of CrN and TiN, from high-resolution EDX analysis and high angle peaks in the XRD pattern. Surface analysis by XPS reveals that Cr mostly exists in the nitride form with minor chromium oxide, and Ti exists mainly in oxynitride state with some TiN. Slight peak position shifts were observed in the XRD pattern. Combined with elemental analysis, it is possible that some oxygen is present in the sample prepared using this method.

Interconversion of CrN to Cr_2O_3 and back to CrN while retaining the inverse opal morphology was demonstrated. However, slight changes in morphology can be observed.

The use of common metal salts to directly obtain macroporous (mixed metal) nitride is demonstrated. This method is shown to be highly versatile and can be integrated into other methods in making porous nitride materials.

REFERENCES

[1] White, G. V.; Mackenzie, K. J. D.; Brown, I. W. M.; Bowden, M. E.; Johnston, J. H. *J. Mater. Sci.*, **1992**, 27, 4294-4299.

[2] Mazumder, B.; Hector, A. L. *J. Mater. Chem.*, **2009**, 19, 4673-4686.

[3] Ramasamy, E.; Jo, C.; Anthonysamy, A.; Jeong, I.; Kim, J.K.; Lee, *J. Chem. Mater.*, **2012**, 24, 1575-1582.

[4] Shi, Y.; Wan, Y.; Zhang, R.; Zhao, D. *Adv. Funct. Mater.* **2008**, 18, 2436-2443.

[5] Li, Y,; Gao, L.; Li, J.; Yan, D. *J. Am. Ceram. Soc.*, **2002**, 85, 1294–1296.

[6] Mangamma, G.; Ajikumar, P. K.; Nithya, R.; Sairam, T. N.; Mittal, V. K.; Kamruddin, M.; Dash, S.; Tyagi, A. K. *J. Phys. D: Appl. Phys.*, **2007**, 40, 4597-4602.

[7] Baxter, D. V.; Chisholm, M. H.; Gama, G. J.; DiStasi, V. F.; Hector, A. L.; Parkin, I. P. *Chem. Mater.* **1996,** *8*, 1222-1228.

[8] Jackson, A. W.; Hector, A. L. J. Mater. Chem., 2007, 17, 1016–1022.

[9] Gray, B. M.; Hassan, S.; Hector, A. L.; Kalaji, A.; Mazumder, B. *Chem. Mater*. **2009**, 21, 4210-4215.

[10] Kaskel, S.; Schlichte, K.; Chaplais G.; Khanna, M. *J. Mater. Chem*., **2003**, 13, 1496–1499.

[11] Yang, M.; Guarecuco, R.; DiSalvo, F. J. *Chem. Mater*. **2013**, 25, 1783-1787.

[12] Yang, M.; Cui, Z.; DiSalvo, F. *J. Phys. Chem. Chem. Phys*., **2013**, 15, 7041-7044.

[13] Giordano, C.; Erpen, C.; Yao, W.; Milke, B.; Antonietti, M. *Chem. Mater.* **2009**, 21, 5136–5144.

[14] Barr, T. L.; Seal, S. *J. Vac. Sci. Technol.* **1995**, 13, 1239.

[15] Moulder, J. F.; Stickle, W. F.; Sobol, P. E.; Bomben, K. D. *Handbook of X-ray photoelectron spectroscopy*; Perkin-Elmer Corporation: Eden Prairie, MN, 1992.

[16] Toth, L. E. *Transition Metal Nitrides and Carbides*; Academic Press: New York, 1971.

[17] Pantea, D.; Darmstadt, H.; Kaliaguine, S.; Roy, C. *Appl. Surf. Sci.*, **2003**, 217, 181-193.

[18] Subban, C. V.; Smith, I. C.; DiSalvo, F. J. *Small*, **2012**, 8, 2824-2832.